

RESEARCH ARTICLE

10.1002/2015JA021773

Key Points:

- Analytical model of low-altitude ENA emissivity depends on local PAD and geometry
- Emissivity-corrected TWINS ion fluxes evaluated using in situ NOAA data
- Global ion precipitation oval comprises multiple smaller-scale structures

Correspondence to:

J. Goldstein,
jgoldstein@swri.edu

Citation:

Goldstein, J., D. V. Bisikalo, V. I. Shematovich, J.-C. Gérard, F. Søråas, D. J. McComas, P. W. Valek, K. LLera, and J. Redfern (2016), Analytical estimate for low-altitude ENA emissivity, *J. Geophys. Res. Space Physics*, 121, 1167–1191, doi:10.1002/2015JA021773.

Received 11 AUG 2015

Accepted 31 DEC 2015

Accepted article online 5 JAN 2016

Published online 6 FEB 2016

Analytical estimate for low-altitude ENA emissivity

J. Goldstein^{1,2}, D. V. Bisikalo³, V. I. Shematovich³, J.-C. Gérard⁴, F. Søråas⁵, D. J. McComas^{1,2}, P. W. Valek^{1,2}, K. LLera^{1,2}, and J. Redfern⁶

¹Space Science Division, Southwest Research Institute, San Antonio, Texas, USA, ²Department of Physics and Astronomy, University of Texas at San Antonio, San Antonio, Texas, USA, ³Institute of Astronomy, Russian Academy of Science, Moscow, Russia, ⁴Institut d'Astrophysique et de Géophysique, Université de Liège, Liège, Belgium, ⁵Birkeland Centre for Space Science, University of Bergen, Bergen, Norway, ⁶Department of Space Studies, Southwest Research Institute, Boulder, Colorado, USA

Abstract We formulate the first analytical model for energetic neutral atom (ENA) emissivity that partially corrects for the global viewing geometry dependence of low-altitude emissions (LAEs) observed by Two Wide-angle Imaging Neutral-atom Spectrometers (TWINS). The emissivity correction requires the pitch angle distribution (PAD) and geophysical location of low-altitude ENAs. To estimate PAD, we create an energy-dependent analytical model, based on a Monte Carlo simulation. We account for energy binning by integrating model PAD over each energy bin. We account for finite angular pixels by computing emissivity as an integral over the pitch angle range sampled by the pixel. We investigate location uncertainty in TWINS pixels by performing nine variations of the emissivity calculation. Using TWINS 2 ENA imaging data from 1131 to 1145 UT on 6 April 2010, we derive emissivity-corrected ion fluxes for two angular pixel sizes: 4° and 1°. To evaluate the method, we compare TWINS-derived ion fluxes to simultaneous in situ data from the National Oceanic and Atmospheric Administration (NOAA) 17 satellite. The TWINS-NOAA agreement for emissivity-corrected flux is improved by up to a factor of 7, compared to uncorrected flux. The highest 1° pixel fluxes are a factor of 2 higher than for 4° pixels, consistent with pixel-derived fluxes that are artificially low because subpixel structures are smoothed out, and indicating a possible slight advantage to oversampling the instrument-measured LAE signal. Both TWINS and NOAA ion fluxes decrease westward of 2000 magnetic local time. The TWINS-NOAA comparison indicates that the global ion precipitation oval comprises multiple smaller-scale (3–5° of latitude) structures.

1. Introduction

The Two Wide-angle Imaging Neutral-atom Spectrometers (TWINS) mission flies two spacecraft in Molniya orbits to achieve stereo imaging of the Earth's magnetosphere [McComas *et al.*, 2009]. The TWINS 1 and 2 imagers measure energetic neutral atoms (ENAs) created by charge exchange in the terrestrial ring current, over the range 1–100 keV/amu, with nominal 4° × 4° angular resolution, at an ~1 min cadence. TWINS stereo ENA observations have advanced our understanding of ring current dynamics at both high and low altitudes [Goldstein and McComas, 2013]. This paper focuses on the near-Earth ENA signal known as the low-altitude emission (LAE). The LAE is a bright feature of ENA images produced by ions in the oxygen exobase [Galand *et al.*, 1998; Roelof and Skinner, 2000; Brandt *et al.*, 2001a]. Observations of LAEs span two decades, via rocket-borne and satellite-based observatories [Søråas and Aarsnes, 1996; Brandt *et al.*, 2001b; Pollock *et al.*, 2001; Mitchell *et al.*, 2003; Pollock *et al.*, 2009; Bazell *et al.*, 2010; Valek *et al.*, 2010; Buzulukova *et al.*, 2013; McComas *et al.*, 2012; Søråas and Sørbo, 2013; Goldstein *et al.*, 2013].

LAEs are a product of the interaction between mirroring or precipitating ions (both auroral and subauroral) and atomic oxygen in the 200–800 km, optically thick O exobase [Galand *et al.*, 1998; Roelof and Skinner, 2000; Brandt *et al.*, 2001a, 2005; Bazell *et al.*, 2010; LLera *et al.*, 2014] (K. LLera *et al.*, Low-altitude emission of energetic neutral atoms: Multiple interactions and energy loss, submitted to *Journal of Geophysical Research*, 2015). Before escaping as ENAs, particles may undergo hundreds of charge exchange and stripping interactions (i.e., changing charge state from ion to neutral or vice versa), which affects their energy and pitch angle distributions (PADs). Because the PADs of these emergent ENAs are highly anisotropic, i.e., sharply peaked at large pitch angles, the ability to image LAEs is strongly dependent on viewing geometry. For a given

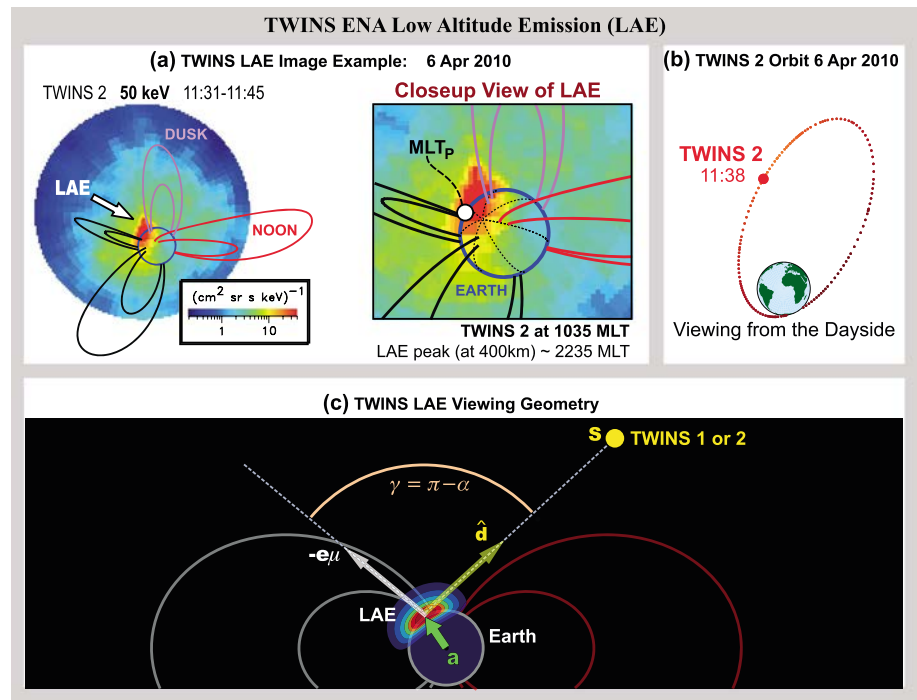


Figure 1. TWINS LAE: example and viewing geometry. (a) Example low-altitude emission image by TWINS 2, 1131–1145 UT on 6 April 2010. Dipole field lines drawn at $L = [4, 8]$ at four cardinal MLT values. Blue circle is the Earth's limb. (b) TWINS 2 orbit and location at UT midpoint of interval. (c) LAE viewing geometry with definition of vectors and angles, adapted from Goldstein *et al.* [2013].

imager location, the apparent ENA brightness varies with source location, because each pixel's line of sight (LOS) samples a different (and narrow) range of local pitch angle. Following Bazell *et al.* [2010], this viewing geometry-dependent LAE brightness function is herein denoted as the emissivity (although we use a slightly different definition; cf. section 2.3). The emissivity function quantifies the portion of an imager's field of view for which the viewing geometry favors LAE imaging, independent of any geophysical (ion flux) variation.

Bazell *et al.* [2010] introduced a thick target approximation (TTA) to simulate ENA propagation in the oxygen exobase and determine LAE emissivity. Their calculation assumes that ion precipitation is globally uniform (independent of latitude and local time) in order to separate viewing geometry effects from actual, i.e., geophysical, variation with magnetic local time (MLT). The emissivity function varies strongly with viewing geometry. For an imager located at magnetic local time MLT_s , the theoretical emissivity is a crescent-shaped region at or within the Earth's limb, centered roughly 12 MLT hours away from the imager, i.e., at $MLT_p = MLT_s + 12$. The emissivity falls off steeply with local time in either direction away from the peak at MLT_p and with increasing latitude away from the limb. Bazell *et al.* [2010] computed emissivity crescents for a weakly disturbed ($Dst \sim -65$ nT) event, yielding a favorable comparison between TWINS-derived ion spectra and simultaneous low-altitude (825 km) in situ data.

Figure 1a shows an example of an LAE observed by TWINS 2 on 6 April 2010 [Goldstein *et al.*, 2013]. This example interval is used as a case study for the remainder of this paper. The LAE is the bright region of high ($\sim 4\text{--}40$ $[\text{cm}^2 \text{sr s keV}]^{-1}$) flux near the Earth's limb. For reference, the blue circle marks the limb at 1 Earth radius (R_E). The highest flux for $r \leq 1 R_E$ is indeed a crescent-shaped region, inside the limb opposite TWINS 2. At the time of the image, TWINS 2 was located (cf. orbit plot of Figure 1b) at geocentric radius $r_s = 5.6 R_E$, magnetic latitude $\Lambda_s = 59.3^\circ$, and $MLT_s = 1035$. The peak limb flux occurs approximately 12 MLT hours from TWINS 2, at $MLT_p \approx 2235$ (cf. close-up view in Figure 1a), and high ENA flux along the limb is localized within ± 3 MLT hours of the peak. Thus, consistent with the theoretical emissivity [Bazell *et al.*, 2010], the observed LAE intensity varies strongly with viewing geometry, specifically with the relative MLT between the imager and the ENA source location. Note that in this study we assume that the LAEs are composed of hydrogen ENAs only, with no contribution from oxygen [Valek *et al.*, 2013]. This assumption is justified for the 50 keV/amu image in Figure 1; the contribution from ~ 0.8 MeV O ENAs is likely to be very small. The goal of ENA image analysis

is to obtain global quantitative information (flux, spatial distribution, and spectra) about the parent ring current ions. For low-altitude ions, it is necessary to factor out the MLT-dependent emissivity function that can obscure the actual local time dependence of the ions. Because of the computational expense of a full simulation of the thick target region [Bazell *et al.*, 2010], for routine LAE analysis it is beneficial to have the choice of a less expensive means of estimating limb ENA emissivity. In this paper we circumvent the numerical calculation of the emissivity function by deriving a simple analytical form based on purely geometrical analysis and with the aid of an analytical model of low-altitude ENA pitch angle that is based on kinetic simulation results.

The rest of this paper is organized as follows. In section 2 we introduce an analytical model of LAE emissivity that depends on viewing geometry and local pitch angle of the ENA source. This emissivity model formulation motivates the rest of the paper. Quantifying the emissivity requires a model for low-altitude ENA pitch angle. Therefore, in section 3 we generate an analytical pitch angle model, based on a computer simulation of the thick target region. In section 4 we apply the emissivity model (with its included pitch angle model) to the TWINS 2 50 keV image of Figure 1. Emissivity-corrected TWINS ion fluxes are compared with simultaneous in situ (NOAA) data in section 5. We find that applying the emissivity correction improves the TWINS-NOAA agreement by as much as a factor of 7 and enables a more direct comparison of single TWINS pixels to individual NOAA ion peaks. In sections 6 and 7 we discuss and summarize our results. Appendix B formulates an ad hoc empirical model of ion precipitation, and Appendix B discusses observations of low-altitude ENAs.

2. Geometrical Emissivity

In this section we introduce an analytical emissivity that depends on the imager location and the local pitch angle (PA) in the low-altitude emission region. The geometrical relations are adopted from Goldstein *et al.* [2013], hereinafter referred to as G13. This section motivates the rest of the paper, by explaining how local particle PA distributions exert control over ENA emissivity.

2.1. TWINS Viewing Geometry

Following G13, TWINS LAE emissions are sampled along or just inside the Earth's limb, according to the viewing geometry shown in Figure 1c. The TWINS spacecraft is located at \mathbf{S} , and the LAE is at $\mathbf{a} \equiv a\hat{\mathbf{r}}$. The unit vector $\hat{\mathbf{d}} \equiv d^{-1}(\mathbf{S} - \mathbf{a})$ points from the LAE to the TWINS spacecraft along the pixel line of sight (LOS); here d is the distance between \mathbf{S} and the LAE source location. It is assumed that the LAE originates at geocentric distance $a = R_E + h$ and has an altitude thickness of b_h , where the selected values $h = 400$ km and $b_h = 300$ km are based on Astrid observations, as in G13. That is, we assume that the LAE originates from the altitude range 250–550 km, which is smaller than the full 200–800 km range for LAEs, but captures the peak emissions observed by the low-altitude Astrid satellite [Brandt *et al.*, 2001a]. Note that we distinguish the LAE limb (at $r = a$) from the Earth surface limb ($r = R_E$). Given this geometry, one may derive expressions for the magnetic latitudes (Λ_a) and local pitch angles (α_a) of TWINS limb-viewing pixels, as a function of azimuthal angle $\varphi_a \equiv \pi(\text{MLT}_a - 12)/12$. These derived equations are found in G13. We note that the limb pitch angle is defined as $\cos \alpha_a = \mathbf{e}_\mu \cdot \hat{\mathbf{d}}$, where \mathbf{e}_μ is a unit vector in the direction of the dipole geomagnetic field.

2.2. Local Pitch Angle Sampling

An example of this geometrical calculation is given in Figure 2. The orbit plot in Figure 2a depicts \mathbf{S} at $(x_S, y_S, z_S) = (2.7, -1.0, 4.8)R_E$, which was the location of TWINS 2 at the time of the LAE image of Figure 1. As noted earlier, we use this example interval as a case study for the remainder of this paper. The red curve marks the Earth's limb ($r = a$) as visible to TWINS 2 from location \mathbf{S} . Figures 2b and 2c plot the calculated Λ_a and its corresponding α_a . Figure 2d shows a plot of the viewing geometry in the meridional plane shared by the imager's local time (MLT_S) and the opposite limb at MLT_P .

From these plots it is clear that each TWINS LOS samples a different value of pitch angle along the limb, and consequently (cf. section 2.3), the ENA pitch angle distribution exerts a strong control on LAE emissivity. LOSs that are closest to the imager (MLT_S) sample southern latitudes and pitch angles in the range $28^\circ - 36^\circ$, a PA interval 8° wide. LOSs that intersect the opposite limb from TWINS (closer to MLT_P) sample northern Λ_a and PA between 29° and 61° , an interval 32° wide. Compared to the southern limb, the pitch angle sampling of the northern limb includes larger (i.e., closer to 90°) PA values and covers a much wider PA range. Consequently, for LAEs with nearly mirroring PADs, more ENAs should be emitted along the LOS of northern limb pixels than southern limb pixels. Indeed, TWINS observations of LAEs from the Southern Hemisphere are rare.

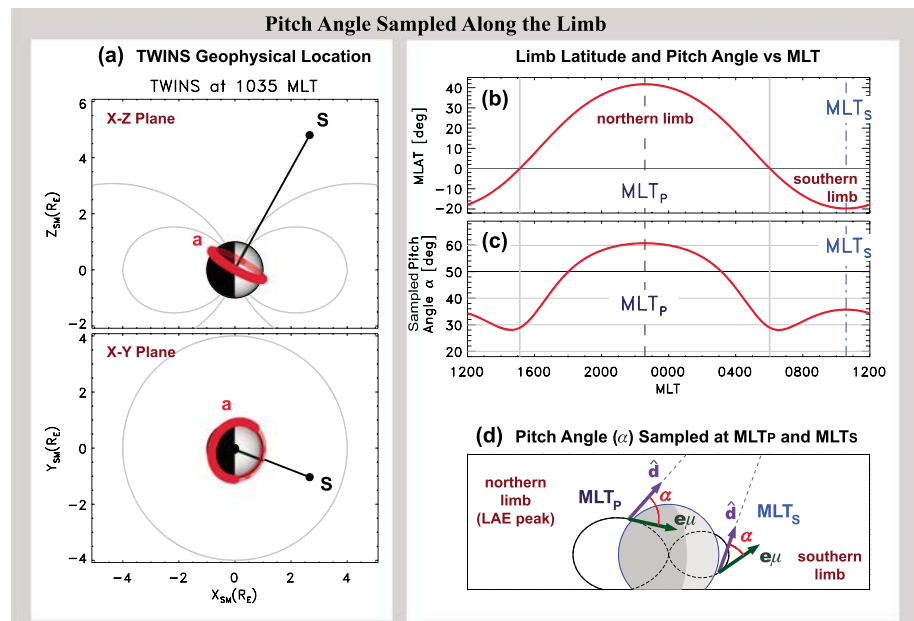


Figure 2. LAE pitch angle sampling by TWINS 2 on 6 April, 1131 – 1145 UT. (a) Spacecraft and limb pixel location. (b) Latitude sampled by TWINS 2 along LAE limb at $R_E + h$. (c) Pitch angle along the limb. (d) Pitch angle sampled in spacecraft meridional plane.

Note the distinction between sampled PA and local PAD. Though LAEs are produced by nearly mirroring ions with highly perpendicular PADs, most LOSs along the limb sample nonmirroring PAs, and thus, the LAE signal does not occur along the entire limb.

2.3. Pitch Angle Control of ENA Emissivity

In this section we demonstrate how sharply peaked, anisotropic ENA pitch angle distributions control LAE emissivity. Figure 3 shows two hypothetical PADs, one isotropic (Figure 3a) and one peaked at 90° (Figure 3c), both normalized to unity. For convenience, we use the simple function $\sin^n \alpha$ for the PAD, with $n = 0$ giving an isotropic distribution and $n > 0$ (in this example, $n = 10$) describing the anisotropic case. It is assumed that the PADs do not vary with geophysical location (MLT, latitude). This simplifying assumption is used in our example to demonstrate the effect of anisotropic PAD on LAE emissivity. The PA control of ENA emissivity would be qualitatively similar for PADs that vary with MLT and latitude. However, we note that the assumption of PA uniformity is also consistent with the model results of section 3.1. (In section 3.1 we discuss the possible validity and consequences of this assumption.)

The example values of α sampled by the TWINS imager (with the viewing geometry depicted in Figure 2) are indicated by the bold red curves. Figures 3b and 3d plot the theoretical LAE emissivity (ϵ) for each of the two hypothetical PADs. The emissivity is herein defined solely in terms of the PAD function. For a sampled value of pitch angle, α_i , the emissivity ϵ_i is simply the value of the PAD function at that pitch angle. Using a normalized PAD function (as in Figure 3) means that the emissivity is likewise normalized, with unity indicating that TWINS limb pixels sample the peak of the PAD. Note that our dimensionless, normalized emissivity differs in definition from that of Bazell *et al.* [2010], which bears the units of differential flux.

For the isotropic case, there is no MLT dependence, i.e., $\epsilon = 1$ along the entire limb even though TWINS only samples a finite range of α . For the anisotropic case, however, the incomplete pitch angle sampling means that TWINS does not capture the PAD peak, and $\epsilon < 1$. The emissivity is sharply peaked at MLT_p , 12 MLT h away from the TWINS location, and for the assumed viewing geometry and $n = 10$ distribution, the peak value is $\epsilon = 0.25$. Thus, even the brightest LAE pixels may represent only a fraction of the peak of the distribution. Moreover, for the case of anisotropic PAD, the LAE has a strong MLT dependence along the limb that would be evident even in the hypothetical case of ion precipitation that is uniformly distributed in MLT. This simple model predicts a steep drop in emissivity with MLT distance from the peak, with the half maximum location ± 3 MLT h from the peak. The emissivity falls from its peak value of $\epsilon = 0.25$ at MLT_p to $\epsilon = 0.07$ at 1800 MLT or 28% of the peak.

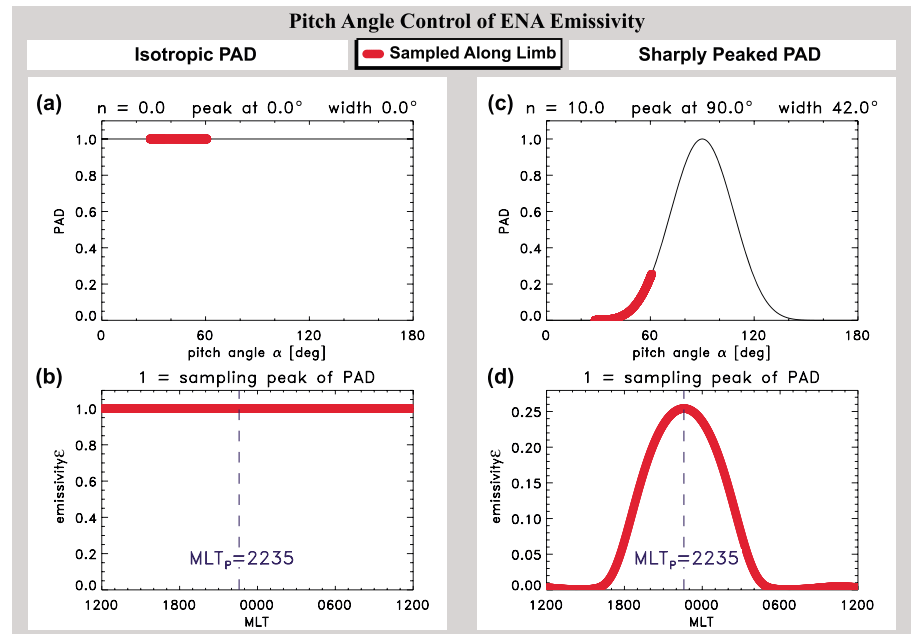


Figure 3. Emissivity (ϵ) dependence on local pitch angle along LAE limb. (a) Isotropic PAD (normalized). Red points: sampling along the limb. (b) Normalized emissivity for isotropic PAD. (c) Anisotropic $\sin^n \alpha$ PAD. (d) Emissivity for anisotropic PAD. Viewing geometry does not sample PAD peak.

To obtain closed-form, analytical solutions, we have (following G13) assumed that each pixel LOS vector \mathbf{a} intersects the LAE region at a single point. In reality, each LOS cuts through a thin (few hundred kilometers) spherical shell of LAE source emissions. Moreover, each pixel subtends a range of limb latitude values. Therefore, in reality each TWINS pixel can include a range of local pitch angle, although that range is limited by the physical size of the ENA source region, which is smaller than the pixel. The effect of discrete (finite-size) pixels is discussed in section 2.4.

2.4. Limb Sampling With Discrete, Offset Pixels

2.4.1. Spatial Discretization

The analysis of sections 2.1–2.3 assumes ideal TWINS pixels. By “ideal pixels” we mean pixels that sample the exact assumed location of the LAE source. In reality, TWINS pixels are of finite angular width (nominally, 4° ; cf. section 5.2 for optional 1° pixels), and each LAE pixel center is offset from the limb by a viewing angle $\Delta\omega_i$ that is generally in the range 0° to 3° .

Limb sampling with discrete, offset pixels is depicted in Figure 4, which plots latitude (Λ) and pitch angle (α) versus MLT, as sampled from the TWINS 2 location depicted in Figure 2. Three assumed locations are shown as follows: the exact limb (blue curve), the actual pixels (red circles), and average offset limb (red curve).

1. The blue curve is the Λ (or α) sampled along the exact geometric location of the LAE limb at $r = R_E + h$.
2. The red points give the centers of the actual TWINS pixels, which are offset from the exact limb. The individual pixel offsets $\Delta\omega_i$ can translate to excursions of tens of degrees in both Λ and α .
3. The red curve shows Λ (or α) along an arc displaced from the true limb by the average (over all pixels) offset $\langle \Delta\omega_i \rangle = 1.2^\circ$.
4. The (asymmetrical) error bars indicate the uncertainty associated with 4° wide pixels. Specifically, each error bar is calculated by applying a $\pm 2^\circ$ shift to each of the (actual) pixel centers. In our formulation -2° is closer to the nadir line, and $+2^\circ$ is closer to the limb. On the limb side, the error bars are bounded by the exact limb (blue curve).

Note that in Figure 4a the pixel centers (red points) are higher in latitude than the exact limb. This results directly from our limb identification algorithm, which only selects pixels whose centers are at or within the exact limb.

The viewing geometry of a pixel is illustrated in Figure 4c. The center of pixel i intersects the limb at latitude Λ_i and samples pitch angle α_i . The pixel edge that crosses the limb at lower latitude Λ_A (i.e., on the left in

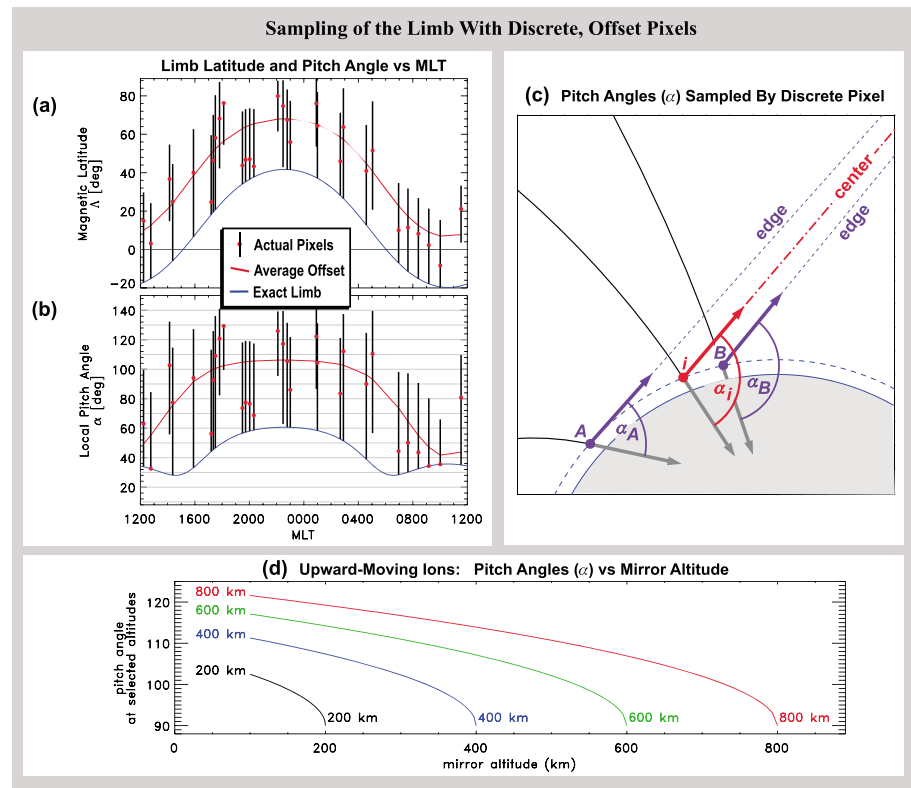


Figure 4. Sampling of LAE limb by discrete, offset TWINS pixels. (a) Limb latitude sampled by actual pixels (black error bars), exact limb (blue), and average offset pixels (red curve). (b) Pitch angle. (c) Viewing geometry of discrete TWINS pixel that samples range of latitudes and pitch angles. (d) Ion pitch angle versus mirror altitude at four selected altitudes spanning the thick target region (200–800 km).

the diagram) samples pitch angle α_A . The higher-latitude (toward nadir) pixel edge samples α_B . From Figure 4 it is evident that a discrete pixel samples a range of values of pitch angle α . Consequently, the geometrical emissivity of pixel i , spanning $[\alpha_A, \alpha_B]$, must be calculated as a definite integral:

$$\epsilon_i = \frac{\int_{\alpha_A}^{\alpha_B} d\alpha g(\alpha) f(\alpha)}{\int_{\alpha_A}^{\alpha_B} d\alpha g(\alpha)}. \quad (1)$$

Here f is the local pitch angle distribution, and g is a weighting function that accounts for possible latitudinal dependence of the ion precipitation. As shown in Figure 4c, the latitude range spanned by the TWINS pixel samples a range of pitch angles $[\alpha_A, \alpha_B]$. An inhomogeneous latitudinal dependence of the ions means that some pitch angles within the pixel are weighted more than the others. Thus, the nonuniform (in latitude) case translates into inhomogeneous sampling of pitch angles within the interval $[\alpha_A, \alpha_B]$. For no spatial dependence, $g = 1$ and

$$\epsilon_i = \frac{1}{\alpha_B - \alpha_A} \int_{\alpha_A}^{\alpha_B} d\alpha f(\alpha). \quad (2)$$

Bazell *et al.* [2010] defined the emissivity as the LAE intensity from a source region that is uniform in both latitude and local time; by this definition we should use $g = 1$. However, TWINS pixels cannot resolve the latitudinal dependence of the ion precipitation region. The use of $g \neq 1$ is a potential means of factoring out this unresolvable latitudinal dependence, to extract an emissivity dependent purely on MLT (cf. section 4.1.2).

Here we are focusing on the subpixel latitudinal dependence but are saying nothing about the subpixel MLT dependence. This rationale for this focus is that for TWINS pixels the latitude sampling is much coarser (tens of degrees) than the MLT sampling (0.2–0.5 h), as shown in Figure 9b. More is said about this topic in section 6.

From Figure 4 it is evident that limb pixels can sample pitch angles greater than 90° . Although we do not have an analytical model of the thick target region, the motion of ions can serve as a helpful conceptual guide.

Ions with $\alpha > 90^\circ$ must have mirrored below the ENA limb, and it is reasonable to question whether particles at these sublimb mirror point altitudes are likely to be lost. Figure 4d shows pitch angle versus mirror altitude (for a dipole field line at $L = 4$) at four selected altitudes spanning the thick target region (200–800 km). For example, at 400 km (blue curve), ions at $\alpha = 107^\circ$ mirror at 200 km (i.e., at the bottom of the thick target region). The farther from 90° the pitch angle is at a given altitude, the lower down the mirror point is. With decreasing ion mirror altitude, the likelihood of being lost increases. Thus, in the altitude range of the thick target region (200–800 km), there is a limited range of pitch angles for which upward moving ENAs can be produced. From Figure 4d, upward moving ions in the 200–800 km range have an approximate pitch angle range of $90^\circ < \alpha < 120^\circ$, which compares well with simulation results for emergent ENAs (cf. section 3).

2.4.2. Energy Discretization

Another discretization effect arises from the finite-size energy bins for TWINS fluxes. The nominal TWINS energy band pass [e.g., Goldstein *et al.*, 2013] is 100% wide; i.e., each energy bin E_j integrates ENA counts from $E_j - 0.5E_j$ to $E_j + 0.5E_j$. Thus, the 1 keV bin spans 0.5–1.5 keV, the 4 keV bin spans 2–6 keV, and so on through the 50 keV bin (25–75 keV). Based on kinetic simulations (cf. section 3.2), we find that the pitch angle distribution of emergent ENAs depends on energy. Thus, the finite energy band-pass ΔE_j can sample a range of different energy-dependent pitch angle distributions $F(\alpha, E)$. To account for this finite ΔE_j , we define an energy-integrated PAD:

$$f(\alpha) = \frac{\int_{E_A}^{E_B} J(E)F(\alpha, E) dE}{\int_{E_A}^{E_B} J(E) dE}, \quad (3)$$

where $[E_A, E_B] = [0.5E_j, 1.5E_j]$. In equation (3) each integrand is weighted by the factor $J(E)$, the flux-versus-energy spectrum (cf. section 3.2.2). Here $J(E)$ is defined as the local ENA flux (at the source). In section 3.2.2 we estimate this quantity using the TWINS-observed ENA flux spectrum.

3. Estimate of ENA Pitch Angle

In the previous section we motivated our study by demonstrating that emissivity is a major effect for LAEs and that it is strongly controlled by the local PADs. Therefore, to quantify the emissivity requires a model of the low-altitude ENA pitch angle distribution. In this section we construct a very basic analytical model for PAD, which depends only on ENA energy (E), based on a computer simulation of the thick target region. Appendix B discusses observations of LAE pitch angle distributions by *Søråas and Aarsnes* [1996] and *Pollock et al.* [2009].

3.1. Computer Simulation of ENA Production

3.1.1. Description of the Code

To estimate the PADs of low-altitude ENAs, we use a direct Monte Carlo computer simulation code [*Hubert et al.*, 2001; *Gérard et al.*, 2000; *Strickland et al.*, 1993]. Though primarily used to estimate the Doppler-shifted Lyman alpha emissions from ENAs produced in the proton aurora [*Galand et al.*, 1998; *Hubert et al.*, 2001; *Gérard et al.*, 2001], the code is also suitable for studying the characteristics of the emergent ENAs themselves. The simulation solves the kinetic equations for electrons, protons, and hydrogen ENAs interacting with thermospheric neutrals (O , O_2 , and N_2) in the auroral region and tracks their PADs as they propagate through the thick target region. The velocity vector redistribution of incident (precipitating) protons includes treatment of magnetic mirroring in a dipole field [*Galand et al.*, 1998; *Galand and Richmond*, 1999], geometric spreading caused by convergent (or divergent) magnetic field lines, and collisions. Our version of the code is modified to output results at nine TWINS energy channels: (1, 4, 8, 12, 16, 20, 25, 30, 50) keV. This modification to output selected energies is a retrofit to a legacy (unsupported) Fortran code. Although in principle the Monte Carlo simulation can be used to replace the TTA correction factor (used later; cf. equation (8), section 5), this additional retrofit is reserved for a future study.

The Monte Carlo simulation offers a very powerful way to study LAEs. This method deserves more attention and discussion than can fit within the scope of this paper, which treats the simulation as a “black box.” Although we ran the simulation for different incident energies (cf. section 3.1.3), we have not yet performed any systematic studies of the variation of the results as a function of inputs or models (e.g., kappa value and exospheric density model). Such testing enables estimation of errors as a function of physical parameters. Lacking this more rigorous testing, our error analysis (below) is limited to calculating the standard deviation of the mean value of each ensemble of simulations. Much more can be said about this method [*Strickland et al.*, 1993; *Gérard et al.*, 2000; *Hubert et al.*, 2001], and much more can be done with this code in future studies.

3.1.2. Model Inputs

The model requires several input parameters: date and time, the $F_{10.7}$ solar index, the AP index, and proton incident energy flux (ϕ_i) and energy (E_i). Continuing to use our case study of 1130 UT on 6 April 2010 (Figure 1), we chose $F_{10.7} = 77.7$ and $AP = 40$ (from OMNIWeb). *Hubert et al.* [2001] used a statistical model to specify their incident (downward) proton energy flux ϕ_i . We chose the arbitrary value $\phi_i = 1 \text{ erg cm}^{-2} \text{ s}^{-1}$, uniformly applied at all grid locations (see description of grid below), because our emissivity function (defined as the fraction of the PAD peak) does not depend on absolute flux values. The incident proton spectrum is a kappa distribution with $\kappa = 3.5$. The input parameter E_i sets the kappa function's peak energy at $E = E_i[1 - 3/(2\kappa)]$.

3.1.3. Simulation Runs and Grid

We ran the simulation for three values of incident proton energy: $E_i = [1, 12, 50]$ keV. The computation time increases with E_i : approximately [1 h, 2 h, 5 h] per grid point at [1, 12, 50] keV, using a MacBook Pro (2.33 GHz processor, 8 GB of RAM). We used a much coarser spatial grid for the 12 keV and 50 keV runs, in part because of this increased computational expense but also because all runs showed only a weak dependence on geographic location, as is discussed in section 3.1.4. The selected spatial domain is a grid of geographic latitude and longitude (GLON) versus altitude (between 126 km and 668 km). We chose our grid to span $40^\circ - 80^\circ$ of latitude and 360° of longitude. For the 1 keV run, we used latitude-longitude spacing of $4^\circ \times 15^\circ$ with overlap at 180° longitude, i.e., an 11 by 25 grid (275 grid points total). For the 12 keV and 50 keV runs, we used $10^\circ \times 45^\circ$ spacing, i.e., a 5 by 9 grid (45 grid points). In total, these three runs took approximately 25 days of computation. The code is not parallelized.

3.1.4. Simulation Results

The simulation results are shown in Figure 5. Figures 5a, 5d, and 5g show the flux of emergent ENAs at 668 km altitude, versus latitude and longitude. The 2-D emergent ENA flux is relatively uniform with only random variations versus location: the standard deviation of the (1 keV, 12 keV, and 50 keV) flux is (9%, 20%, and 20%), as perhaps expected given the uniform incident energy flux ϕ_i . Note that these deviations are proportional to $N_G^{-0.5}$, where N_G is the number of grid points. Figures 5c, 5f, and 5i quantify the ENA pitch angle distributions at 668 km, as follows. At each grid point, the code yields a pitch angle distribution at 4° PA resolution. For each grid point we fit a spline of the emergent PAD to the function $n\bar{\alpha}$. Here $\bar{\alpha} \equiv (\alpha - \alpha_0 + \pi/2)$, where the α_0 parameter allows for a PAD whose peak is not at 90° . Figures 5c, 5f, and 5i are 2-D plots of the value of n for this fit. These are high values of n , corresponding to highly perpendicular PADs, consistent with ENAs produced near ion mirror points. Each plot is annotated with the mean values of n and α_0 and their standard deviations. As with the fluxes, over the 2-D grid the n value has no clear spatial dependence, with a standard deviation of (17%, 35%, and 36%) at (1 keV, 12 keV, and 50 keV). The PAD peak location α_0 is even more uniform, with a standard deviation of $\leq 1\%$ at all energies. This relatively weak (and random) variation of emergent ENA PADs suggests that our model (cf. section 3.2) need not depend on latitude or MLT.

By inspection of Figures 5c, 5f, and 5i, the PAD peak location α_0 has at most a mild energy dependence: α_0 varies by less than 2% as energy increases from 1 keV to 50 keV. To test whether this small α_0 variation is dependent on the spatial grid, we rebinned the 1 keV run to $8^\circ \times 45^\circ$ and found no change in α_0 . In contrast, the parameter n does have an energy dependence, falling by nearly 50% over the same energy range. This energy dependence is discussed below. At all energies, the large n values indicate PADs that are very sharply peaked (anisotropic). Figures 5b, 5e, and 5h plot each model run's fluxes (versus PA), for all grid points on the same axes. The blue dots give the mean values at each pitch angle, and the red curve is a $\sin^n \bar{\alpha}$ fit to the entire data set. The plot is annotated with the fit parameters n and α_0 , which are comparable to the mean values from the 2-D plots. The energy dependence of n is evident in these PAD plots: as energy increases, n falls by roughly 50%, and the simulated PAD becomes slightly broader. Between 1 keV and 50 keV, n falls from about 400 to 200, with corresponding full width half maxima increasing from 6.7° to 9.5° , i.e., by about 2.8° . It is reasonable to question the significance of the differences in the low-energy and high-energy PADs, which would possibly be difficult to observe in real particle distributions. In this paper we choose to use the simulation's energy-dependent n to create an energy-dependent model of ENA PADs, in part because the broadening of the PAD with energy is consistent with theoretical expectations, as discussed in section 3.2. An alternate approach (which we do not herein choose) would be to discard the simulation's energy dependence of n and combine the results from all energies into a single average value of n .

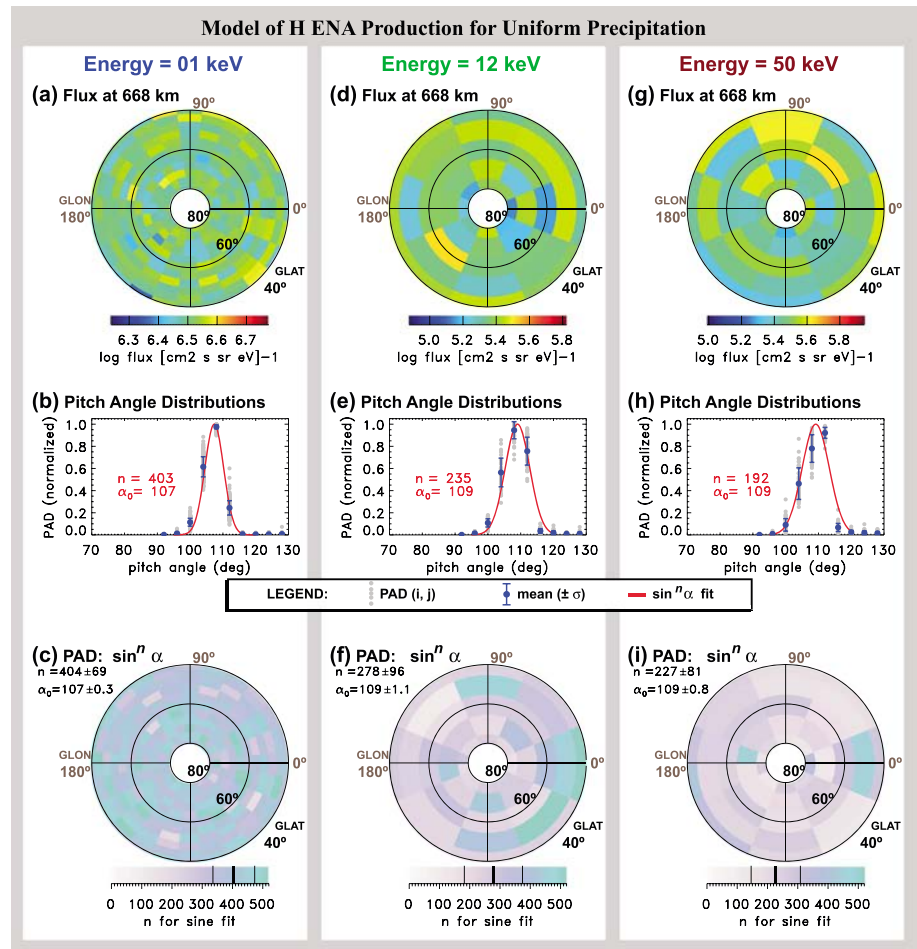


Figure 5. Output of Monte Carlo simulation for [1, 12, 50] keV. (a, d, and g) Flux at 668 km altitude, geographic coordinates. (b, e, and h) PADs of all grid points with $\sin^n \alpha$ fit. (c, f, and i) Two-dimensional maps of n fit parameter. Black lines in color bar show mean n and standard deviation.

3.2. PAD Model Versus Energy

3.2.1. Analytical Model of LAE Pitch Angle

In this section we compile the computer simulation results (section 3.1) to obtain a simple model of ENA pitch angle. Our model assumes that ENA pitch angle distributions are spatially uniform, i.e., depend only on the energy of the emergent ENAs and not on latitude or MLT. It is worth briefly discussing the validity and significance of this approximation, which is based on the simulation output that (to zeroth order) does not contain a systematic geographical dependence. In nature, any spatial dependence would result from asymmetries in the neutral exospheric density (and thus collision cross sections). Larger exospheric densities would cause higher ENA fluxes and more sharply peaked PADs. The Monte Carlo simulation estimates exospheric oxygen density using the MSIS86 model [Hedin, 1987, 1991], which has a factor of ~ 2 day-night density asymmetry, at 400 km altitude and for latitudes between 40° and 80° . For the simulation results of section 3.1, the dayside sector is centered at $\sim 7.5^\circ$ GLON. There does not appear to be a systematic dayside asymmetry in ENA flux (Figures 5a, 5d, and 5g) or in ENA pitch angle (Figures 5c, 5f, and 5i). Although there is the hint of an asymmetry (favoring $\sim 0^\circ$ GLON) in the PAD for 12 keV (Figure 5f), because this asymmetry does not appear in the 1 keV or 50 keV distributions, it can be attributed to random fluctuations. Thus, despite the \sim factor-of-2 diurnal asymmetry in the MSIS86 density model, the simulation output has no systematic (across all energies) dayside asymmetry. We leave it for a future study to quantify the effect of exospheric density asymmetries larger than the factor of ~ 2 in the MSIS86 model.

To parameterize our model, we continue using the $\sin^n \alpha$ function. Our ENA PAD model parameters n and α_0 are shown in Figure 6a. Individual points of n (red) and α_0 (blue) are the mean values from the PAD plots of

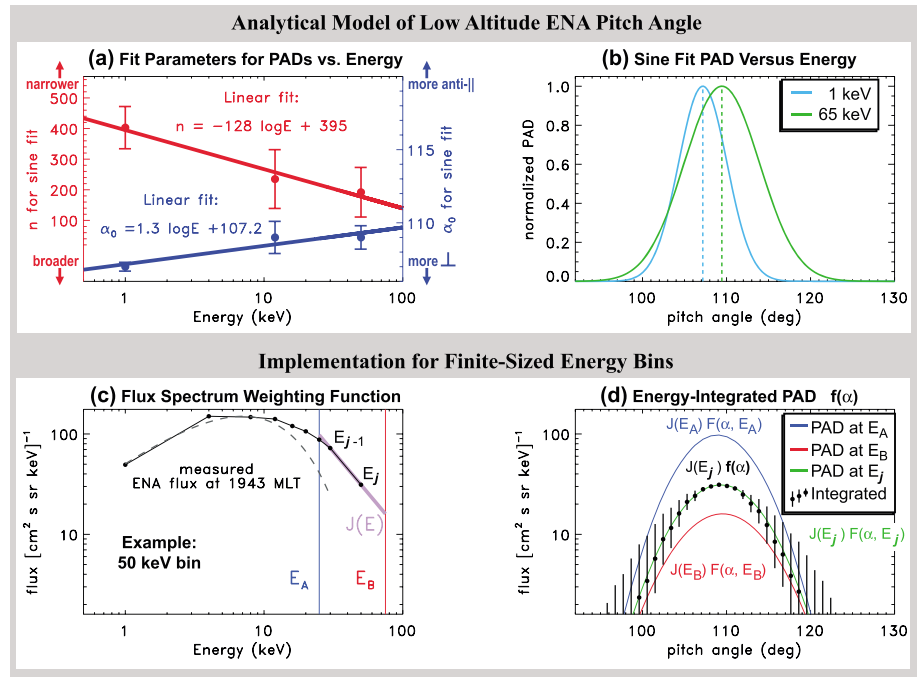


Figure 6. Model of ENA PAD based on simulation output of Figure 5. (a) Model fit parameters. (b) Model PAD plotted at [1, 65] keV. (c) Determination of $J(E)$ for 50 keV pixel at 1943 MLT. (d) Resulting energy-integrated PAD (black) and single-energy PADs at (E_A, E_j, E_B).

Figures 5b, 5e, and 5h, and the error bars on these values are their standard deviations (same as Figures 5c, 5f, and 5i). The red and blue lines are linear fits to n and α_0 (respectively) versus $\log E$. The model n maintains the energy dependence noted earlier, falling by 59% (from 395 to 163) between 1 keV and 65 keV. On the other hand, the model α_0 increases by only 2% over the same energy range, from 107° to 109° . The progression (with energy) from more narrow PADs located at smaller α_0 to slightly broader PADs at larger α is illustrated in Figure 6b.

While a particle is an ENA, it travels ballistically across magnetic field lines. Because the Earth’s magnetic field diverges with increasing altitude, an ENA with 90° pitch angle will arrive at a neighboring field line with a larger component of upward field-aligned motion, which for Northern Hemisphere LAEs means $>90^\circ$ pitch angle. When the ENA is reionized, this $>90^\circ$ PA translates into an upward (antiparallel) ion bounce motion. Multiple successive neutralization and ionization interactions thus gradually convert a mirroring ion into an emergent ENA with $\alpha > 90^\circ$ [Galand and Richmond, 1999] (K. LLera et al., submitted manuscript, 2015).

With this process in mind, the trends in model n and α_0 are consistent with expected particle behavior in the thick target region [Galand et al., 1998], where a particle experiences numerous charge exchange and stripping (i.e., neutralization and ionization) interactions that gradually convert a mirroring ion into an emergent ENA with $\alpha > 90^\circ$. The stripping collisional cross section increases with E up to about 60 keV [Basu et al., 1987; Goldstein et al., 2013], meaning that more energetic particles have a shorter mean free path; these particles will undergo more stripping collisions and therefore should have broader PADs (i.e., lower values of n). More energetic particles will travel farther upward along the field while they are ions, both because the charge exchange cross section decreases with ion energy and more energetic ions travel faster. These hotter particles increase their PA at a slightly higher rate (per kilometer of altitude) than colder particles. Thus, with increasing E , the PAD broadens, and the PAD peak location α_0 migrates farther from 90° , in the antiparallel (upward) direction.

3.2.2. Implementation for Finite Energy Bins

To account for the energy discretization by finite-size TWINS energy bins, we use equation (3) to calculate the energy-integrated PAD as

$$f(\alpha) = f_0^{-1} \int_{E_A}^{E_B} J(E) \sin^{n(E)} \bar{\alpha}(E) dE, \quad (4)$$

where $\bar{\alpha}(E) = \alpha - \alpha_0(E) + \pi/2$ and $f_0 = \int J(E) dE$ (integrated from E_A to E_B). The integration limits span the 100% wide energy bin centered at E_j : $[E_A, E_B] = [0.5, 1.5]E_j$. The energy-dependent values of $n(E)$ and $\alpha_0(E)$ are calculated using the analytical PAD model of section 3.2.1.

In equation (4) the integrand is weighted by the local ENA flux versus energy $J(E)$. We estimate this spectral weighting function as a two-point linear fit (in log-log space) to the observed (per-pixel) energy spectrum. At each energy bin (E_j) and pixel the fit is constrained by two-point arrays of flux (J) versus energy (E) at or adjacent to E_j . For energy E_j , this fit is

$$J(E) = J_{j-1} \left(\frac{E}{E_{j-1}} \right)^{m_j}, \quad (5)$$

where

$$m_j = \frac{\log(J_j/J_{j-1})}{\log(E_j/E_{j-1})}. \quad (6)$$

For $j = 0$, these two formulas require the substitution $j \rightarrow j + 1$. An example of this fitting procedure is shown in Figure 6c. Plotted in black is the ENA flux spectrum measured by TWINS 2 at 1943 MLT and 1131–1145 UT on 6 April 2010 (cf. Figure 1). For reference, the dashed line shows a Maxwellian ($kT = 7$ keV). For the energy bin centered at 50 keV, $[E_{j-1}, E_j] = [30, 50]$ keV and $[J_{j-1}, J_j] = [72, 32]$ ($\text{cm}^2 \text{sr s keV}^{-1}$). Using these values in equation (5) yields the fit $J(E)$ plotted in lavender, which spans the entire 25–75 keV bin. A different such $J(E)$ is calculated for each pixel along the limb, since the LAE spectrum is observed to vary with MLT [Goldstein *et al.*, 2013].

There is a technical complication associated with using the TWINS-observed per-pixel ENA flux to estimate the local ENA flux $J(E)$. The observed flux J_{obs} is itself the product of the local ENA flux times the local pitch angle distribution, averaged over the energy bin, i.e., $J_{\text{obs}} \propto \int_{E_A}^{E_B} J(E) f(\alpha_i, E) dE$. In general, this would lead to “double counting” of the PAD in the integrals of (4). However, one can easily show that for steeply rising or falling spectra (e.g., Figure 6c) the observed flux versus energy is dominated by the local flux spectrum, not the PAD variation with energy. In this case, the per-pixel PAD may be approximated by its energy bin-averaged value f_j . In the example of Figure 6c, the difference between calculating J_{obs} with an energy-dependent PAD versus the bin-averaged PAD is $<1\%$. Therefore, $J_{\text{obs}} \approx f_j J(E)$, and the PAD dependence of J_{obs} can be factored out of both numerator and denominator of (4). In the case of a relatively flat spectrum, for which the approximation fails, one can revert to the single-energy PAD.

With the spectral weighting function determined, the integral in (4) can be calculated. We use a simple rectangular approximation with 51 log-spaced energy steps spanning $[E_A, E_B]$. An example for the 50 keV bin is shown in Figure 6d. Each solid curve (blue, red, and green) shows the single-energy PAD $F(\alpha, E)$, scaled by the ENA flux at that energy. That is, each solid curve is a plot of the integrand of (4) at a different value of energy E . The blue and red curves show the scaled PADs at the endpoints (E_A and E_B) of the numerical integration. The green curve is the scaled PAD at $E_j = 50$ keV, the center of the energy bin. The black dots show the energy-integrated PAD obtained from equation (4). The error bars are obtained via error propagation of the standard deviation of the analytical PAD model (Figure 6a). For this particular example, the energy-integrated PAD (black dots) is not significantly different than the single-energy PAD (green curve) that would have been obtained by simply applying equation (4) to the energy bin center E_j . In the general case, how different the integrated PAD is depends on the per-pixel $J(E)$ spectrum and the energy bin. The energy integration is the correct method to account for the full range of energy-dependent PADs captured by a TWINS pixel.

4. TWINS Emissivity Estimate

In section 2 we showed how the TWINS viewing geometry samples a limited range of ENA pitch angles along the limb. For anisotropic PAD and a given viewing geometry, this means that the LAE emissivity ϵ depends strongly on MLT along the limb. In section 3 we used simulations to formulate an energy-dependent model for the PAD, which is anisotropic and centered at pitch angles slightly above 90° , as expected. In this section we use the preceding analysis to estimate ϵ for our case study TWINS 2 image of Figure 1.

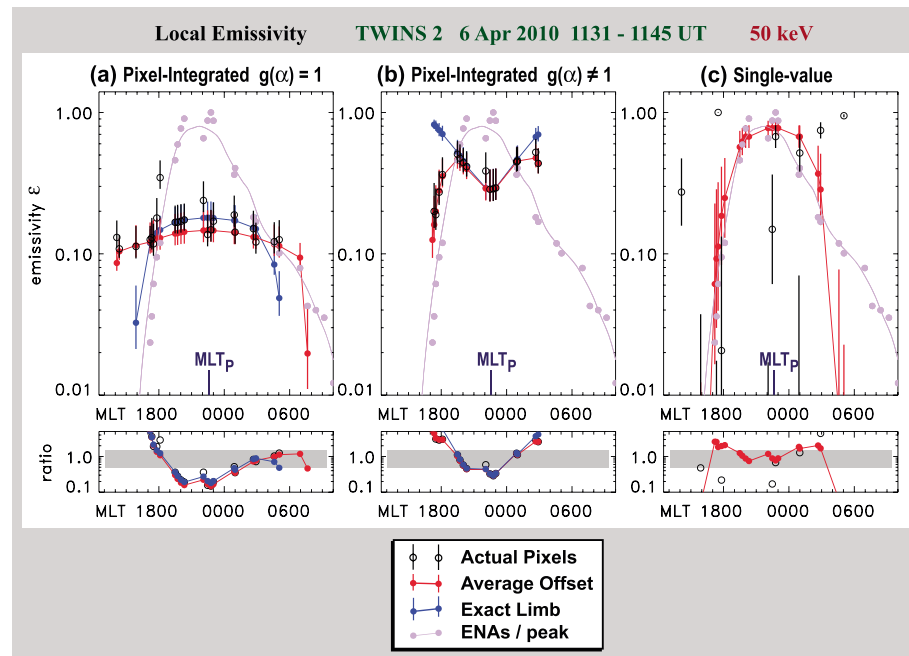


Figure 7. Emissivity (ϵ) curves, TWINS 2, 1131–1145 UT, 6 April 2010. (a) Pixel-integrated ϵ for $g = 1$ at exact limb (blue), actual pixels (black), and average offset limb (red). Lavender curve: normalized ENA curve $f_{\text{ENA}} \cdot \epsilon / f_{\text{ENA}}$ (bottom). (b) Pixel-integrated ϵ for $g \neq 1$. (c) Single-value ϵ .

4.1. Calculated Emissivity

To estimate LAE emissivity for the 50 keV TWINS 2 image from 1131 to 1145 UT on 6 April 2010, we perform nine different computations, all using energy-integrated PADs as in section 3.2.2. The results of these different calculations are compared in section 4.2.1 to determine the optimum method. For all emissivity values, error bars are obtained via error propagation of the standard deviation of the analytical PAD model (Figure 6a). The results are shown in Figure 7 and described in the following text.

4.1.1. Pixel-Integrated, Uniform $g(\alpha)$: Three Versions

First, we assume that ion precipitation is uniform in latitude (consistent with the emissivity definition of *Bazell et al.* [2010]); i.e., we assume $g = 1$ and use equation (2). The integration uses a five-point Newton-Cotes algorithm (the “int_tabulated” function in Interactive Data Language). The resultant pixel-integrated emissivity curves are plotted in Figure 7a, for three different assumed limb pixel locations: exact limb (blue), actual pixels (black, open circles), and average offset pixels (red), as described in section 2.4.1. The blue circles are for pixels whose fields of view span $\pm 2^\circ$ from the exact geometric limb. The black circles result from integration across the actual pixel fields of view, using the individual pixel offsets $\Delta\omega_i$. Note that there are no filled black circles, although there are a handful of instances of open black circles plotted on top of blue dots. The red circles are for pixels within $\pm 2^\circ$ of the all-pixel average offset ($\langle \Delta\omega_i \rangle = 1.2^\circ$) limb. The lavender curve is the observed 50 keV ENA flux along the limb, normalized to unity for comparison with the emissivity curves (section 4.1.4).

These three pixel-integrated, $g = 1$ emissivity curves are all similar to each other in general shape and magnitude. The red and blue curves rise more or less smoothly to a broad peak centered roughly at $\text{MLT}_p = 2235$ MLT. The black circles follow this same general shape, but with more scatter associated with the offsets of individual pixels. In the range 1700–0300 MLT, the blue and red curves agree within their error bars; outside of this core MLT range the blue curve diverges steeply downward from the red curve. In this same core MLT range, the actual pixel points (open black circles) also generally agree with the other two curves, with two exceptions at about 1800 MLT and 2200 MLT. The explanation for the general agreement among the three different curves is that despite the differences in the assumed pixel center locations, the 4° pixel fields of view are broad enough to result in significant overlap of the integration limits for the three methods.

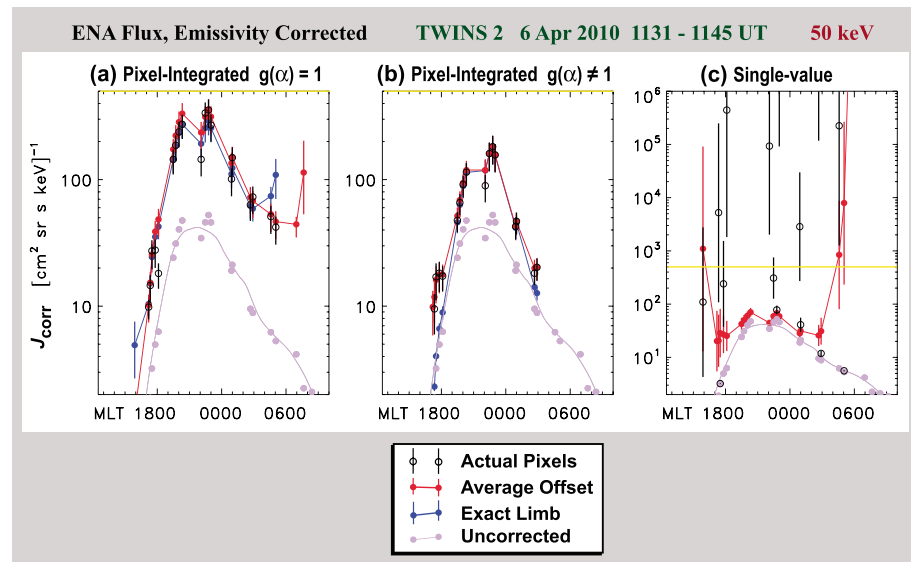


Figure 8. Emissivity-corrected ENA fluxes using ϵ curves of Figure 7. Yellow line: plot range of Figures 8a and 8b.

The presence of a broad peak centered at MLT_p is predicted by our simple, single-point emissivity model (sampled at the exact limb) of Figure 3d. However, in contrast to the simple model, the emissivity curve using the finite-pixel integration formula of equation (1) has a much more gradual drop in emissivity with MLT distance from the peak. The simple model predicts the emissivity at 1800 MLT to be 28% of the peak at MLT_p (cf. section 2.3). The pixel-integrated emissivity at 1800 MLT is 82% (or 88%) of the value at MLT_p for the blue (or red) curve.

4.1.2. Pixel-Integrated, Nonuniform $g(\alpha)$: Three Versions

The TWINS 4° pixels span tens of degrees of geophysical latitude, a range much larger than that of the ion precipitation. If the ion distribution versus latitude is known, it may be factored out to yield an emissivity curve that depends solely on MLT . Lacking this information, for this study we derived an ad hoc empirical model of ion precipitation based on the statistical study of *Hardy et al.* [1989], as described in Appendix A. We set $g = G(\alpha, MLT)$, where the latter function is that of equation (A4), but normalized and mapped to a corresponding distribution in sampled pitch angle α for the span of each finite-size pixel. With nonuniform g specified, we perform the integration of equation (1). In Figure 7b we plot emissivities along the exact limb (blue), actual pixels (black), and average offset pixels (red). As was the case for the $g = 1$ curves in Figure 7a, the three $g \neq 1$ curves of Figure 7b agree within their error bars in a core MLT range, in this case 1900–0100 MLT . The red and black curves agree with each other at all MLT s. All three curves have a local minimum at MLT_p that results from the fact that those TWINS limb pixels sample latitudes above the main precipitation oval (cf. Appendix A). The lavender curve does not have this local minimum, most likely because either the actual precipitation oval spans a slightly different latitude range than the model or the high-latitude boundary of the oval is less well defined than the model.

4.1.3. Single-Value Emissivity: Three Versions

Instead of integrating over the full 4° field of view of each pixel, we sample the PAD at a single location Λ_i . The weighting function is then $g = \delta(\alpha - \alpha_i)$, and equation (1) reduces to $\epsilon_i = f(\alpha_i)$, i.e., the single-point (0 pixel size) case of section 2.3. The results are plotted in Figure 7c. The average offset emissivity curve (red points) is qualitatively similar to the $g = 1$ pixel-integrated curves (Figure 7a), with a broad peak centered roughly at MLT_p , although the drop with MLT distance from the peak is comparatively steep. There are no blue points plotted; the exact limb values are all approximately zero ($\epsilon_i < 10^{-29}$) because the values of α sampled are $\leq 60^\circ$ (cf. Figure 4b), far outside the range of α for which the 50 keV PAD—peaked at 109° —is nonnegligible. The very large degree of scatter in the actual pixel emissivities (black circles) results from the variability in the individual pixel offsets (Figure 4b), which produces a pixel-to-pixel randomness in the particular values of α sampled. The scatter is such that roughly half the actual pixel emissivities fall outside the plot range. This randomness is smoothed out for the finite-pixel emissivities (Figures 7a and 7b) that each sample a larger range of α , leading to significant overlap of the various $\int d\alpha$ integrations.

4.1.4. Shape Comparisons: ENA Versus Emissivity

If the modeled emissivity (ϵ) is accurate, and if the MLT dependence of the observed ENA flux is caused by viewing geometry alone, then the ϵ function should reproduce the global shape of the ENA flux versus MLT curve.

In this section we compare the shapes of the computed emissivities with that of the observed 50 keV ENA flux versus MLT. In each plot of Figure 7, the normalized 50 keV ENA flux (f_{ENA}) is plotted in lavender. The circles give the per-pixel values, and the solid line is a cubic spline (smoothed by a 2.4 MLT hours boxcar average) to guide the eye. As a qualitative measure of agreement, the lower panels plot the ratios ϵ/f_{ENA} for each of the individual curves; in these plots, the gray colored region indicates agreement to within $\pm 50\%$. For the nine different computed versions of ϵ , we find a mixture of good, moderate, and poor agreement between ϵ and f_{ENA} :

Figure 7a. Although the pixel-integrated ϵ_i curves do have a broad peak at MLT_p , they exhibit a much milder dependence on MLT than f_{ENA} in the range 1700–0300 MLT. Only the exact limb (blue) emissivity shows some level of agreement with f_{ENA} , but only below 1700 MLT and above 0300 MLT.

Figure 7b. For all three ϵ_i curves there are local minima at MLT_p , in contrast with the broad peak (centered at MLT_p) in f_{ENA} . As noted above, this discrepancy may be caused by differences between the model and actual precipitation ovals. For local times 1600–1900 MLT the slopes of the red and black curves follow that of f_{ENA} , although the values of ϵ exceed that of the normalized ENA curve f_{ENA} .

Figure 7c. The two plotted single-point ϵ curves show two dramatically different levels of agreement with f_{ENA} . The enormous scatter in the actual pixel emissivities (black circles) disagrees strongly with the relatively smooth f_{ENA} curve. On the other hand, the shape of the average offset (red) curve agrees quite well with f_{ENA} for 1900–2300 MLT. As noted above, the exact limb emissivities (blue points) were all negligible and are not plotted.

The closest shape agreement seems to be for the single-point average offset (red) emissivity curve; however, as will be discussed in section 4.2, this red curve produces corrected ENA fluxes that are unrealistically high at some MLTs.

Based on these ϵ -to- f_{ENA} shape comparisons, we conclude that either the observed ENA flux's MLT dependence is not entirely caused by viewing geometry or our simple calculation is too crude to fully capture the observed emissivity versus MLT. The former possibility appears to be unverifiable without more empirical information. The latter possibility, if true, suggests that because emergent ENA pitch angle distributions are so sharply peaked, uncertainties in our method can produce very large variations in ϵ . These uncertainties include (1) per-pixel knowledge of the latitude (and thus, the sampled α) of the source region and (2) errors in the analytical PAD model. Latitude uncertainty is unavoidable, as discussed earlier, and our attempt to mitigate it via a nonuniform $g(\alpha)$ achieved reasonable agreement only in a limited MLT range. Another way to minimize latitude uncertainty is to use 1° pixel images (cf. section 5.2). Model error is likewise inevitable because of the shortage of published observations of the PADs of emergent ENAs.

4.2. Corrected ENA Flux

The emissivity herein represents the fraction of the PAD peak that is sampled by a TWINS pixel. To correct the ENA flux (J_{ENA}) for this viewing geometry effect means dividing it by ϵ :

$$J_{\text{corr}} = J_{\text{ENA}} [\epsilon]^{-1}. \quad (7)$$

Figure 8 plots values of J_{corr} along the exact limb (blue), actual pixels (black), and average offset pixels (red), for the pixel-integrated and single-valued emissivities. The uncorrected ENA flux is plotted in lavender.

We next compare these several different calculations of J_{corr} to choose a single method for further analysis. In section 4.1.4 we compared the shapes of $\epsilon(\text{MLT})$ curves with normalized ENA flux curves. This purely shape-based comparison was performed under the assumption that the observed MLT dependence of ENA flux is at least in part caused by emissivity. In this section we are calculating corrected ENA fluxes; i.e., we are attempting to use the estimated emissivity curves to factor out the emissivity dependence. In principle, J_{corr} should be the global ENA distribution (along the limb) without viewing geometry effects. In practice (see below), this correction is of course limited and imperfect. Therefore, in the remainder of this section we merely discuss whether the corrected curves appear to be physically reasonable and/or consistent with each other. In section 5 we attempt to judge the accuracy of J_{corr} by converting it to ion flux and comparing with NOAA data.

4.2.1. Pixel-Integrated J_{corr}

The pixel-integrated J_{corr} curves are found in Figures 8a and 8b, respectively, for the uniform ($g = 1$) and nonuniform ($g \neq 1$) PAD weighting functions. The group of three $g = 1$ (or $g \neq 1$) curves all agree within their error bars in the range 1800–0300 MLT (or 1900–0100 MLT), as expected from the agreement found for the corresponding groups of emissivity curves (Figure 7). The two groups of three J_{corr} curves are also comparable: except for a factor of ~ 2 difference in magnitude, the $g = 1$ and $g \neq 1$ curves are all quite similar in shape between 1900 and 0100 MLT. This agreement is somewhat surprising given the differently shaped ϵ_i curves for the uniform versus nonuniform g found in Figure 7. However, it is worth noting that the pixel-integrated emissivities all vary by less than a factor of 2 in this MLT range. The similarity of the six different J_{corr} curves is encouraging given the large uncertainties in the emissivity calculation (section 4.1.4).

Based on the similarity between the two main variations ($g = 1$ and $g \neq 1$) of pixel-integrated emissivity calculation, we conclude that either method is acceptable to obtain corrected ENA flux. We choose the $g = 1$ method for further analysis, because the $g = 1$ method employs an emissivity definition more consistent with that of *Bazell et al.* [2010] and does not require an additional empirical model (e.g., the H89 model of Appendix A). Next we consider the three different $g = 1$ curves (blue, black, and red), which are all quite similar in shape and magnitude. We reject the exact limb method (blue curve) because although this curve is smooth and well behaved, the exact limb pixels are displaced (on average) tens of degrees away (in both Λ and α) from the actual pixels. On the other hand, even though in principle the actual pixel values (black points) should be most accurate, the scatter in these points is undesirable (and may introduce additional unquantifiable error associated with the relatively large pixel size). Therefore, we choose the $g = 1$ average offset method (red curve) for analysis of 4° images (section 5.1), to avoid pixel-to-pixel scatter from individual offsets while still placing the pixel centers in the correct locations, on average. We choose the $g = 1$ actual pixel method (black dots) for analysis of 1° images (section 5.2) because the pixel-to-pixel offset scatter is much less for the higher-resolution images (Figure 10).

4.2.2. Single-Value Method

The single-value J_{corr} is plotted in Figure 8c, for actual pixels (black) and average offset pixels (red). Neither of these methods is selected for further analysis. The pixel-to-pixel scatter in the actual pixel emissivities yields variations in J_{corr} that span several orders of magnitude. Only half of the black points are included in the plot range, which has been expanded by a factor of 2000 relative to the previous two plots. Whereas the average offset (red) curve avoids the actual pixel scatter, the central (1800–0300 MLT) correction to the ENA flux is minimal (a factor of 2 at most), and the curve contains factor-of-1000 flux increases outside of 1800–0300 MLT that are probably unrealistic.

5. TWINS-NOAA Ion Flux Comparison

Thus far, we have determined a method to calculate J_{corr} , which is the global low-altitude ENA flux with the viewing geometry dependence at least partially factored out. In this section we extend this analysis. We use the pixel-integrated, uniform-precipitation ($g = 1$) emissivity (section 4) to obtain corrected TWINS ion fluxes. We compare these ion fluxes to simultaneous in situ data from NOAA 17 for two TWINS pixel sizes, 1° and 4° .

5.1. Comparison Using 4° Pixel Image

Figure 9a plots TWINS 2 flux versus MLT from 1131 to 1145 UT on 6 April 2010. The blue circles are the emissivity-corrected ENA flux $J_{\text{corr}} = J_{\text{ENA}}(\epsilon)^{-1}$ of equation (7); dividing by ϵ applies the emissivity correction. The background-subtracted ENA flux J_{ENA} is obtained by estimating the background as the minimum ENA flux along the limb. The ENA flux J_{ENA} is converted to ion flux J_{ion} using

$$J_{\text{ion}} = J_{\text{ENA}} \frac{F_c}{\epsilon} \left[1 + \frac{\sigma_s}{\sigma_c} \right]. \quad (8)$$

As in G13, F_c is a geometric, pixel size correction accounting for the fact that the vertical scale of the LAE source is smaller than the TWINS pixel [*Brandt et al.*, 2001a; *Goldstein et al.*, 2013]. Note that there are two different geometric corrections being performed in this paper. The emissivity correction attempts to account for the viewing geometry effect in which different pixel lines of sight sample different values of a very sharply peaked PAD. On the other hand, the pixel size correction F_c scales up the flux in an attempt to account for a source

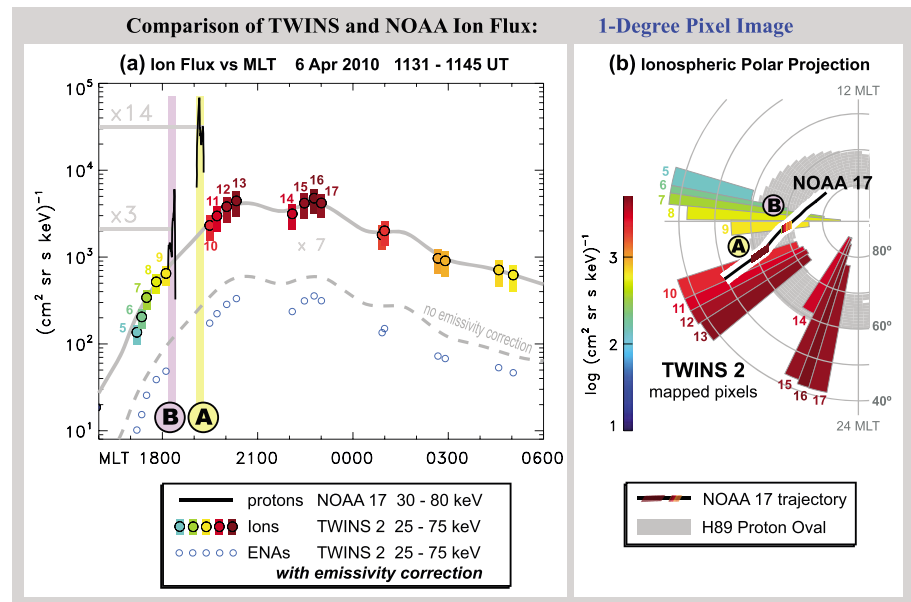


Figure 9. TWINS-derived ion flux compared to simultaneous NOAA 17 peaks A and B (Appendix B). (a) ENA flux (blue), uncorrected ions (gray dashed), corrected flux (colored dots, numbered), and NOAA flux (black). (b) TWINS and NOAA fluxes mapped to polar ionosphere. H89 proton oval indicated.

region smaller than the pixel; the value of F_c for our case study is 8.16. The σ_c and σ_s are (respectively) the charge exchange and stripping cross sections. The factor in square brackets is from the TTA approximation of Bazell et al. [2010] for pixel-averaged flux. We make no correction to TTA for finite-sized energy bins; however, Goldstein et al. [2013] showed that the magnitude of this correction is $<3\%$. Note that $J_{\text{ion}} = J_{\text{corr}} F_c [1 + \sigma_s / \sigma_c]$.

Figure 9a plots the resulting TWINS 2 ion flux values as color-coded circles. The colored error bars indicate the uncertainty arising from the standard deviation of the model PAD (cf. Figures 6a and 6d), added in quadrature to the Poisson counting errors. The thick gray line is a cubic spline fit (smoothed by a 1.2 MLT hours boxcar average) to guide the eye. Note that the average (over MLT) value of our emissivity is 0.12, so that the correction (dividing by ϵ) introduces a factor of 7 increase. For reference, the uncorrected ion flux is plotted (dashed gray line). The shape of the corrected curve is not significantly different from the uncorrected curve. There is only a factor of ~ 2 difference between the uncorrected ion flux (dashed line) and the corrected ENA flux (blue circles).

For comparison, NOAA 17 proton flux data are overplotted, showing the two main peaks (“A” and “B”) that occurred during 1138–1148 UT (cf. Figure B1b). To aid the comparison, Figure 9b is an ionospheric polar projection (MLT versus latitude). The TWINS flux pixels are mapped onto the plot using their actual locations, and latitude edges defined as the $\pm 2^\circ$ viewing angle range, as in Figure 4a. The NOAA 17 proton fluxes are overplotted along the satellite’s polar orbit trajectory. The flux color bar used for both TWINS and NOAA is the same as Figure 9a. The TWINS pixels are numbered for ease of reference.

We now compare TWINS and NOAA 17 fluxes. In Figure 9b, NOAA precipitation peak A is closest to TWINS pixel 10 (red), and NOAA peak B is closest to TWINS pixel 9 (yellow-orange). For these two conjunctions, the NOAA ion fluxes are 3 to 14 times larger than those derived from TWINS. In Figure 9a, the mean value of each NOAA peak is indicated (thick gray horizontal lines). NOAA peak A (or B) has flux 14 (or 3) times larger than that of TWINS pixel 10 (or 9). It is unsurprising that the NOAA fluxes are higher than those of TWINS. In Figure 9b, each TWINS pixel spans tens of degrees of magnetic latitude and 0.2–0.5 h in MLT. The NOAA data contain spatial structures too small to resolve with TWINS pixels. Averaged over the large area of a TWINS pixel, such smaller-scale structures are smoothed out, resulting in a lower mean flux. With this understanding, agreement in absolute flux to within an order of magnitude is encouraging. Using the full numerical calculation of LAE emissivity, Bazell et al. [2010] obtained TWINS fluxes 2 to 9 times smaller than simultaneous Defense Meteorological Satellite Program (DMSP) in situ flux values. We have achieved a comparable level of agreement (factor of 3 to 14) using a simpler and less computationally expensive method.

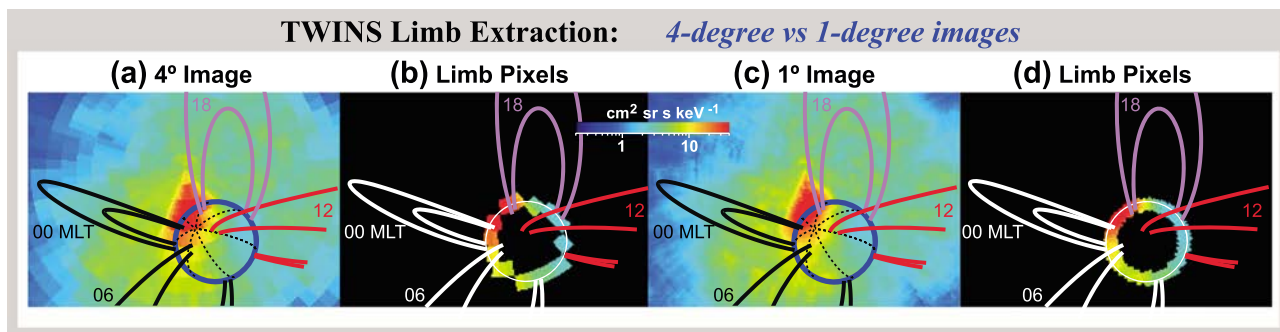


Figure 10. TWINS limb pixels for 4° and 1° oversampled pixel images. (a, b) ENA image and limb pixels, 4° image. (c, d) ENA image and limb pixels, 1° image, avoiding jagged limb sampling.

For reference, the predicted oval from the H89 empirical model (Appendix A) is indicated by the gray shaded region, bounded by $\Lambda = \Lambda_p \pm \Delta\Lambda_p$. As discussed in Appendix B and evident in Figure 9b, the latitude range spanned by the two NOAA peaks (A and B) agrees with the H89 model's prediction for the extent of the ion oval.

In our previous study of this event (G13), the lack of an emissivity estimate severely limited the MLT range of valid TWINS ion fluxes. Thus, G13 compared TWINS flux, averaged over all limb values within 20% of the global peak, to NOAA flux averaged over both peaks A and B. The NOAA “A+B” flux was 20 times larger than the TWINS all-limb-averaged flux. The new analytical estimate for ϵ , while still quite limited, has allowed an expansion of the MLT range of TWINS fluxes and thus a more direct comparison between individual pixel TWINS fluxes and individual NOAA peaks (TWINS pixel 9 with NOAA peak B and pixel 10 with peak A). Using the emissivity correction, the obtained level of agreement in absolute flux is improved by a factor of 1.4 (for peak A) to 7 (for peak B) compared to the uncorrected method.

5.2. Comparison Using 1° Pixel Image

The TWINS angular field of view is usually discretized into 4° by 4° pixels. Figure 10a shows a close-up view of the 4° TWINS 2 image from 1131 to 1145 UT on 6 April 2010. Figure 10b is the same image but showing only the limb pixels. Here limb pixels are defined as those whose centers lie within an annulus bounded $r = R_E + h$ (outer), and by the critical offset angle ω_c (inner), inside of which there are no solutions to the geometrical equations [Goldstein *et al.*, 2013]. The limb pixels follow a jagged curve rather than a smooth one because 4° pixels are comparable in size to the limb curve. From an imager at 5.6 R_E geocentric distance (Figure 2a), the LAE limb diameter ($2a$) spans 21.5° or 5.4 pixels across. The jagged sampling produces large scatter in the sampled latitude and pitch angle and bunching of sampled MLT values (Figure 4). MLT bunching is evident in Figure 9; e.g., there is a gap of nearly 2 MLT hours between pixels 13 and 14. As discussed in section 5.1, using 4° pixels means the LAE source location is uncertain by tens of degrees of latitude, and derived per-pixel ion fluxes are artificially low in comparison to in situ data.

In an attempt to mitigate latitudinal uncertainty and pixel-averaged flux reduction, we next compute emissivity-corrected ion fluxes using 1° pixels. To explain how 1° images are made requires a brief description of the instrument [McComas *et al.*, 2009, 2012]. Each of the TWINS imagers has two collimating sensor heads, mounted on a rotating actuator that sweeps through 180° and back to capture ENAs in a cone-shaped field of view. Each sensor head measures incoming ENAs in two orthogonal directions: the instrument's 1-D imaging angle λ (parallel to the collimator plates) and the actuation angle β . The TWINS imagers do report β position with 1° accuracy, and the direct-events imaging angle information can (in principle) be discretized into arbitrary-sized pixels. Thus, it is possible to create images with 1° × 1° pixels for count rates below the telemetry rate [Valek *et al.*, 2010; McComas *et al.*, 2012; Valek *et al.*, 2013, 2014]. However, these smaller pixels oversample the instrument angular resolution in both dimensions, as follows. First, the slit camera has an angular (versus β response curve that is 4° wide at full width at half maximum (FWHM). Second, owing to foil scattering and MCP/anode signal spreading, the imaging angle has an intrinsic, energy-dependent FWHM angular resolution that is ~16° at 1 keV and levels off to ~7° at energies above ~10 keV [Goldstein *et al.*, 2013]. Thus, sorting ENA counts into 1° × 1° bins is an oversampling of the intrinsic $\lambda \times \beta$ instrument angular resolution, which for 50 keV ENA images is ~ 4° × 7°. What is then gained by this oversampling? The smaller β pixels

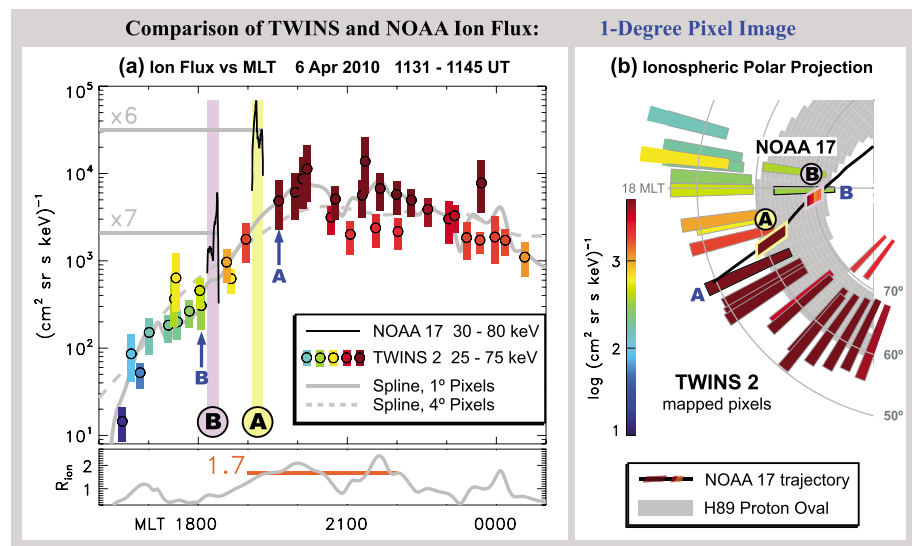


Figure 11. TWINS 2 and NOAA 17 ion flux, for higher-resolution 1° TWINS pixels. (a) TWINS ion flux (colored dots), NOAA flux (black), spline of 1° TWINS flux (gray), and spline of 4° flux (gray dashed). $R_{ion} \equiv J_{ion}(1^\circ) \div J_{ion}(4^\circ)$, showing factor of ~2 ratio between 1900 and 2200 MLT (bottom). (b) TWINS and NOAA fluxes mapped to polar ionosphere, with H89 proton oval indicated.

more closely conform to the limb’s circular shape, reducing the jaggedness of the limb curve (see below). Oversampling an image has also been shown in some cases to slightly improve effective resolution [e.g., Fruchter and Hook, 2002; Bai et al., 2011].

Figure 10d shows the LAE limb at 1° resolution, with much reduced jaggedness of the sampled limb curve, and oversampling of the ENA signal in both latitude and MLT. At this higher resolution the limb annulus contains 422 pixels, as compared to the 30 pixels of the 4° image. Figure 11 shows ion fluxes calculated using the 1° image. To facilitate comparison with high-flux NOAA data obtained above 55° latitude, we filtered the 422 limb annulus points by retaining only points that satisfy the criterion $\epsilon \leq 0.25$, resulting in 37 points between 1600 and 0100 MLT. Using 1° images, the individual pixel fluxes are not consistently closer to the fluxes of NOAA peaks A and B. NOAA peak A has flux 6 times larger than corresponding TWINS 1° pixel A (labeled in blue), a factor-of-2 improvement compared to the 4° pixel comparison. NOAA peak B’s flux is 7 times that of TWINS pixel B, a factor-of-2 worse comparison than the 4° case.

However, with the smaller 1° pixels, the highest (peak) derived ion fluxes are a factor of ~2 higher than for the 4° pixel image, as follows. The gray solid line is a cubic spline (smoothed by a 0.8 MLT hour boxcar average) of the 1° flux. The gray dashed line is a spline (smoothed by 1.2 MLT hours) of the 4° flux, taken from Figure 9. The ratio of the 1° and 4° spline flux curves is R_{ion} , plotted in the bottom panel. In the range 1900–2200 MLT, i.e., the region of peak flux, the mean R_{ion} is 1.7. The highest flux values derived from 1° pixels are thus larger than those derived from 4° pixels, perhaps indicating that oversampling at 1° may be a slight improvement for LAE imaging at higher energies. The highest TWINS fluxes ($\sim 10^4$ [cm² sr s keV]⁻¹) are comparable to the mean NOAA flux (averaged over both peaks) of ~ 6000 [cm² sr s keV]⁻¹ (cf. Appendix B).

As in the previous figure, in Figure 11b the predicted oval from the H89 model is given by the gray region. The TWINS 1° pixels that overlap the H89 model oval have higher fluxes (that agree better with NOAA data), and the pixels fully outside the H89 oval are generally (with just a few exceptions) lower.

6. Discussion

Our result shows that it is possible to correct—at least partially—for the viewing geometry dependence of low-altitude ENA emission using a simple analytical model. Such correction requires knowledge of two attributes of the emergent ENAs: pitch angle distribution and geophysical location. There are unavoidable uncertainties in both of these quantities.

To estimate the ENA pitch angle, we have formulated a simple, energy-dependent model. We estimate the uncertainty in the PAD based on the standard deviation of our analytical model. However, the analytical PAD model is based solely on the output of a Monte Carlo simulation whose accuracy we do not attempt to quantify. Lacking observations of low-altitude ENA pitch angle with which to compare the simulation output, we rely on two facts: (1) the Monte Carlo simulation has been successfully used to model the proton aurora [Hubert *et al.*, 2001; Gérard *et al.*, 2001] and (2) the trends in PAD versus energy are consistent with the physics of particles in the thick target region [Galand *et al.*, 1998].

Geophysical location of the ENA source is determined using the geometrical analysis of Goldstein *et al.* [2013]. However, for the standard 4° TWINS pixel, the latitude uncertainty can be tens of degrees. From where in the pixel does the ENA signal originate? We investigated this uncertainty in three ways:

1. We defined a pixel-integrated emissivity to account for the range of source pitch angles within each pixel.
2. We performed nine different emissivity calculations, six pixel integrated and three single valued. Three of the pixel-integrated curves incorporated a weighting function to account for an inhomogeneous distribution of ion precipitation within the pixel.
3. Emissivity-corrected ion fluxes were calculated at 1° pixel resolution, for comparison to those of the standard 4° pixel images.

Despite these significant uncertainties, the emissivity correction obtains a level of agreement with NOAA ion fluxes that is as much as a factor of 7 better than the uncorrected method of G13, and higher-resolution images may be preferable. As noted earlier, the highest (peak) flux values derived from 1° pixels are a factor of ~2 higher than for the 4° pixels. Given that higher fluxes agree better with NOAA data, it is arguable that the 1° oversampled image generally yields more accurate flux values. Higher fluxes for smaller pixels is consistent with the idea that pixel-averaged fluxes can be artificially low because smaller-scale structures are smoothed out (cf. Figure B1e). Nonetheless, the intrinsic angular resolution of the instrument apparently limits the improvement obtained from 1° oversampling. Large latitudinal uncertainty also makes for a more imperfect conjunction between TWINS and NOAA. Analyzing smaller pixels mitigates but does not remove these sources of error. Aside from the built-in imager resolution, 1° pixels are still larger than the ion structures being imaged. NOAA peaks A and B each span only ~3–5° of magnetic latitude (cf. Figure B1e). TWINS 1° pixels are 10–15° wide in latitude (Figure 11b). Increased pixel resolution does not eliminate the intrinsic limitations of comparing pixel-averaged flux to “ground truth” in situ data, using an imager with finite resolution.

Throughout this paper we have focused on the subpixel latitudinal dependence of the parent precipitating ions and the ENAs produced from them. This focus is not intended to imply that there is only a latitudinal dependence of precipitation. Quite the contrary, it is well established that ion precipitation also shows MLT structure smaller than a TWINS pixel can resolve [Hardy *et al.*, 1989; Frey *et al.*, 2003; Newell *et al.*, 2010]. In fact, it is the MLT dependence that we hope to reveal with TWINS data, by factoring out the much less quantifiable latitudinal dependence. Because of a combination of the TWINS orbital/viewing geometry and the way the imager functions, TWINS image pixels span a much large range in geophysical latitude (tens of degrees) than MLT (0.2–0.5 h); i.e., the resolution of the latitude dimension is much worse than the MLT dimension. Consequently, TWINS pixels may include in their field of view large regions for which there is essentially zero ion precipitation. Our analysis examines possible ways to correct for this situation.

Comparison with in situ data is a natural means of evaluating our analytical model of emissivity. Agreement in absolute flux to within an order of magnitude is reasonable given the intrinsic difference between pixel-averaged and in situ-measured quantities. It is likewise remarkable that a simple analytical model for ENA emissivity can agree with NOAA data nearly as well as the full numerical computation of Bazell *et al.* [2010] did with DMSP. The comparison with in situ data does not quite validate the method in general. The narrow peaks (A and B) measured by NOAA essentially represent only two points when compared with TWINS fluxes. Our study demonstrates that the emissivity correction can work for real cases, but additional validation is needed. For example, in our comparison with NOAA data we chose to use the uniform ($g = 1$) version of pixel-integrated emissivity. We justified this choice by arguing that uniform precipitation is more consistent with the existing definition of emissivity [Bazell *et al.*, 2010] and slightly more practical in that it needs no empirical precipitation model. Indeed, the $g = 1$ calculation produced agreement with NOAA data that is better than would have been obtained from the $g \neq 1$ case. This statement is based on the fact that in Figure 8, emissivity-corrected ENA flux J_{corr} is higher for $g = 1$ than for $g \neq 1$, and higher TWINS fluxes agree better with NOAA data. Nonetheless, for a different case study, the nonuniform ($g \neq 1$) computation may fit

the data better. Therefore, it seems reasonable to question our somewhat subjective choice of $g = 1$ and test it in future validation studies. Once validated, it is our plan to routinely use emissivity analysis to characterize the global evolution of energy-dependent ion flux in an ensemble of storms. By applying our emissivity correction method to sequences of TWINS images, we can obtain a measure of the global ion flux across a broad range of MLT, versus time. By analyzing multiple storms, we can quantify the activity dependence of the time-varying global ion flux.

Perhaps equally important as validation, such global-to-local comparisons help reveal cross-scale structure. For both TWINS and NOAA, ion flux decreases with MLT west of about 2000. Coupled with the approximate equality of absolute flux, this qualitative agreement suggests that the global ion precipitation region comprises numerous mesoscale and fine-scale ion structures (that presumably vary on minute time scales), as has indeed been observed in numerous proton auroral images [e.g., Frey *et al.*, 2003]. TWINS pixels that span 10 or more degrees of latitude cannot capture these smaller structures, but they do provide necessary, quantitative global contextual information.

7. Summary

We have formulated the first analytical model for low-altitude ENA emissivity that corrects for the viewing geometry dependence of low-altitude ENAs and have evaluated our model via comparison of TWINS 2 imaging data with simultaneous NOAA 17 in situ measurements. We have demonstrated that the method can work for real cases, although additional validation is needed. Our analytical model enhances the information that can be obtained from LAE images, without the need for a more computationally expensive simulation of the thick target region.

The emissivity correction requires knowledge of both the pitch angle distribution and geophysical location of the ENA source. To estimate ENA pitch angle, we created an analytical model that depends only on energy, based on the output of a Monte Carlo simulation of the proton aurora, for three energies spanning the TWINS range: 1 keV, 12 keV, and 50 keV. With increasing energy, the model PAD broadens (becomes less anisotropic) and migrates toward more upward directed ENAs. We account for finite-width TWINS energy bins by integrating the model PAD function over each energy band pass, weighted by the observed per-pixel flux spectrum. We account for the effect of discrete angular pixels that are offset from the true geometric LAE limb (at altitude h) by computing per-pixel emissivity as an integral over the pitch angle range sampled by the pixel. Because a TWINS pixel can span 10 or more degrees of latitude (and thus sampled pitch angle), we investigated the geophysical location uncertainty by performing nine different emissivity calculations, six pixel integrated and three single valued. Three of the pixel-integrated emissivity curves incorporate an empirical weighting function to account for an inhomogeneous distribution of ion precipitation within the pixel. Comparison of these different emissivity curves indicates that the optimum method assumes uniform precipitation within the pixel, using either actual or average offset pixels. The assumption of nonuniform precipitation, while conceptually more consistent with the understanding that TWINS pixels are larger than the source region, relies upon an empirical model of ion precipitation rather than the actual ion distribution and can produce a local minimum at the MLT where TWINS observes the LAE peak.

For one case study image obtained by TWINS 2 during 1131–1145 UT on 6 April 2010, we derived emissivity-corrected ion fluxes from images at two pixel angular resolutions: 4° and 1° . We compared the TWINS-derived ion fluxes to simultaneous NOAA 17 in situ data. The agreement in absolute flux is improved by as much as a factor of 7, compared to the uncorrected method of our previous study [Goldstein *et al.*, 2013]. The highest 1° resolution fluxes are a factor of 2 higher than for the 4° pixels, consistent with the idea that pixel-derived fluxes can be artificially low because smaller-scale ion structures are smoothed out, and indicating a possible slight advantage to oversampling the instrument-measured LAE signal. Both TWINS and NOAA ion fluxes show a decrease westward of 2000 MLT. The TWINS-NOAA comparison indicates that the global ion precipitation oval comprises multiple smaller-scale structures.

Our result is valid for hydrogen LAEs. The PAD model is based on the Monte Carlo simulation that only considers electrons, protons, and H atoms, and the $g \neq 1$ weighting function is based on the average proton aurora compiled by Hardy *et al.* [1989]. Future work may extend the model to consider oxygen LAEs [Valek *et al.*, 2013, 2014, 2015] as well.

Appendix A: Ad Hoc Empirical Model of Ion Precipitation Based on *Hardy et al.* [1989]

In this appendix we derive an ad hoc empirical model for the 2-D distribution of ion precipitation, versus latitude (Λ) and MLT. The model is based on the $Kp = 4$ statistical proton map of H89 [*Hardy et al.*, 1989]. The H89 results are binned into integer values of Kp between 1 and 6. We chose $Kp = 4$ as the nearest integer matching our case study interval's $Kp = 4.3$ (1131–1145 UT, 6 April 2010).

The procedure for deriving this model is as follows. From a scanned digital (PDF) copy of the published paper, we extracted the $Kp = 4$ proton map as a JPEG. The JPEG pixels were converted to ion flux using the published color bar. An algorithm identified the latitude (Λ_p) of the peak flux at each MLT, and Fourier expanded to obtain

$$\Lambda_p = \sum_{n=0}^2 C_n \cos(n\varphi) + S_n \sin(n\varphi), \tag{A1}$$

where $\varphi = \pi(\text{MLT} - 12)/12$, $C_n = [68.8, 5.5, 1.4]$, and $S_n = [0.0, -1.0, -0.3]$. The half maximum peak width ($\Delta\Lambda_p$) was similarly identified, and Fourier expanded as

$$\Delta\Lambda_p = 11.12 - 1.25 \cos(2\varphi). \tag{A2}$$

The MLT-dependent flux at the peak (a_p) also required Fourier expansion:

$$a_p = \sum_{n=0}^2 A_n \cos(n\varphi) + B_n \sin(n\varphi), \tag{A3}$$

where $A_n = [7.9, 0.2, 1.1]$, $B_n = [0, -0.3, -0.2]$, and a_p is in units of $10^6 \text{cm}^{-2} \text{sr}^{-1} \text{s}^{-1}$. These MLT-dependent parameters Λ_p , $\Delta\Lambda_p$, and a_p were used to define a Gaussian in latitude:

$$G(\Lambda, \text{MLT}) = a_p \exp \left[-4 \ln 2 \frac{(\Lambda - \Lambda_p)^2}{\Delta\Lambda_p^2} \right]. \tag{A4}$$

This ad hoc function is compared to the published H89 proton data in Figure A1. The published $Kp = 4$ proton map (extracted from the digital copy of the paper) is plotted in Figure A1a versus MLT (noon at the top) and Λ from 50° to 90° . The corresponding model $G(\Lambda, \text{MLT})$ of (A4) is plotted in Figure A1b. The absolute flux difference between the data and model is plotted in Figure A1c. The mean difference over the entire distribution is 5% of the peak flux.

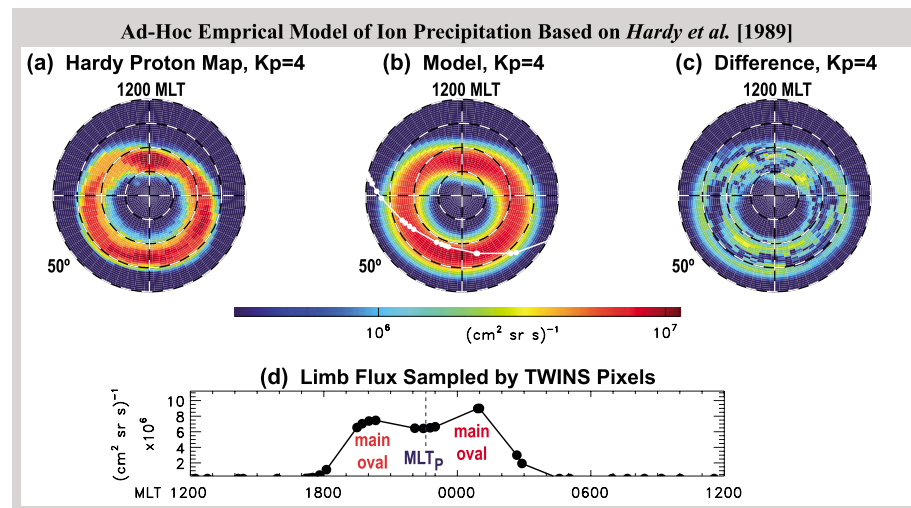


Figure A1. Ad hoc H89 empirical model of *Hardy et al.* [1989] statistical ion precipitation. (a) Proton map ($Kp = 4$). (b) Analytical fit to proton map. (c) Difference between proton map and model. (d) Model limb flux sampled by TWINS pixels, 1131–1145 UT on 6 April 2010.

In section 4.1.2 the model $G(\Lambda, \text{MLT})$ is used to define a dimensionless weighting function $g(\alpha)$ for numerical integration of pitch angle distributions in order to derive the emissivity according to equation (1). We briefly describe the procedure for this application. First, the function G is normalized at each MLT by setting $a_p = 1$. Second, the latitude distribution at each pixel, specified by $G(\Lambda)$, is mapped to a corresponding pitch angle weighting function $G(\alpha)$. The one-to-one mapping of sampled Λ to sampled α is performed geometrically using the equations of Goldstein *et al.* [2013]. The specific equation used to map from Λ to α is

$$\cos \alpha = -\frac{h_\mu}{a^3 d} \left\{ \frac{3}{2} \cos 2\Lambda (\xi - \rho_a) + (3 \sin^2 \Lambda - 1) \delta z \right\} \quad (\text{A5})$$

where h_μ , ξ , ρ_a , and δz are fully defined by a set of nine equations from Goldstein *et al.* [2013], which are not repeated here.

It is worth mentioning that the H89 model characterizes precipitating flux, integrated over all energies. In general, different energy ranges may have different spatial distributions. Therefore, using the integrated H89 proton map for individual TWINS energy bins may introduce additional errors to the emissivity analysis.

When $G(\Lambda, \text{MLT})$ is sampled at the locations of TWINS-observed limb pixels, there results a two-peaked distribution, with a local minimum at MLT_p (i.e., the MLT value opposite that of the TWINS spacecraft), as follows. The locations of the TWINS pixels (using the all-pixel-average offset; cf. Figure 4) are overplotted onto Figure A1b as the white curve. The fluxes sampled along this curve are plotted in Figure A1d. The local minimum at MLT_p occurs because those TWINS pixels sample latitudes above the peak of the main precipitation oval. The two nearby peaks represent the intersection of the TWINS visible limb with the highest fluxes in the main oval. The two peaks have different flux values in Figure A1d because of the MLT dependence of the function a_p in (A3). When the function G is normalized, as it is for use in (1), these two peaks bear the same flux and thus weight the emissivity integration equally (producing the symmetric peaks in Figure 7b).

In addition to serving as a PA weighting function in ϵ calculations (herein), a parameterized representation of the statistical proton maps of Hardy *et al.* [1989] has other possible uses. An H89 model can facilitate comparisons among precipitating ion spectra derived from both imaging (TWINS) and in situ data (e.g., NOAA) and serve as a useful counterpoint to statistical analysis of low-altitude ENAs. Work is already underway to advance this ad hoc treatment to a full empirical model that includes Kp dependence in its fit coefficients.

Appendix B: Observations of LAE PADs

In this study we employed a Monte Carlo simulation code to estimate the energy-dependent pitch angle distributions of low-altitude ENAs. Such simulations are computationally expensive and (as with any model) are most informative when complemented by observations. This appendix discusses observations of low-altitude PADs.

One of the few reported pitch angle resolved observations of low-altitude ENAs was by the Poleward Leap sounding rocket, made near a proton arc on 11 November 1983 [Søråas and Aarsnes, 1996]. Figure B1a plots the sounding rocket-observed PAD (black dots) for ENAs between 50 and 80 keV (center energy at 65 keV), at 454 km. The red curve gives a fit to the $\sin^n \alpha$ function used in our study, which yields $n = 24$ and $\alpha_0 = 83^\circ$. The observed PAD of Figure B1a is sharply peaked ($n = 24$) at $\alpha_0 = 83^\circ$; i.e., most of the protons are moving downward in altitude along the field line, although a significant fraction are moving upward. Although it is indeed expected that low-altitude ENA pitch angle distributions are highly anisotropic, these Poleward Leap observations of mostly downward moving ENAs cannot be directly used to constrain a PAD model for use by TWINS (as in section 3.2.1). However, with some modeling, these observations may be indirectly useful. In the thick target region (200–800 km altitude), the pitch angle of a downward moving ENA can be increased by the cumulative influence of multiple charge-changing interactions in a convergent magnetic field [Søråas and Aarsnes, 1996; Galand *et al.*, 1998; Hubert *et al.*, 2001]. A thick target transport model might provide the means to convert the PAD observed by Poleward Leap at 454 km into a model PAD at the 800 km upper limit of the thick target region. Development of a code that might perform this conversion is underway [LLera *et al.*, 2014] (K. LLera *et al.*, submitted manuscript, 2015).

Next, we examine whether low-altitude observations by the National Oceanic and Atmospheric Administration (NOAA) Polar-orbiting Operational Environmental Satellites (POES) can help to constrain further the low-altitude ENA pitch angle distributions. From our previous study (G13), NOAA 17 data are available for our

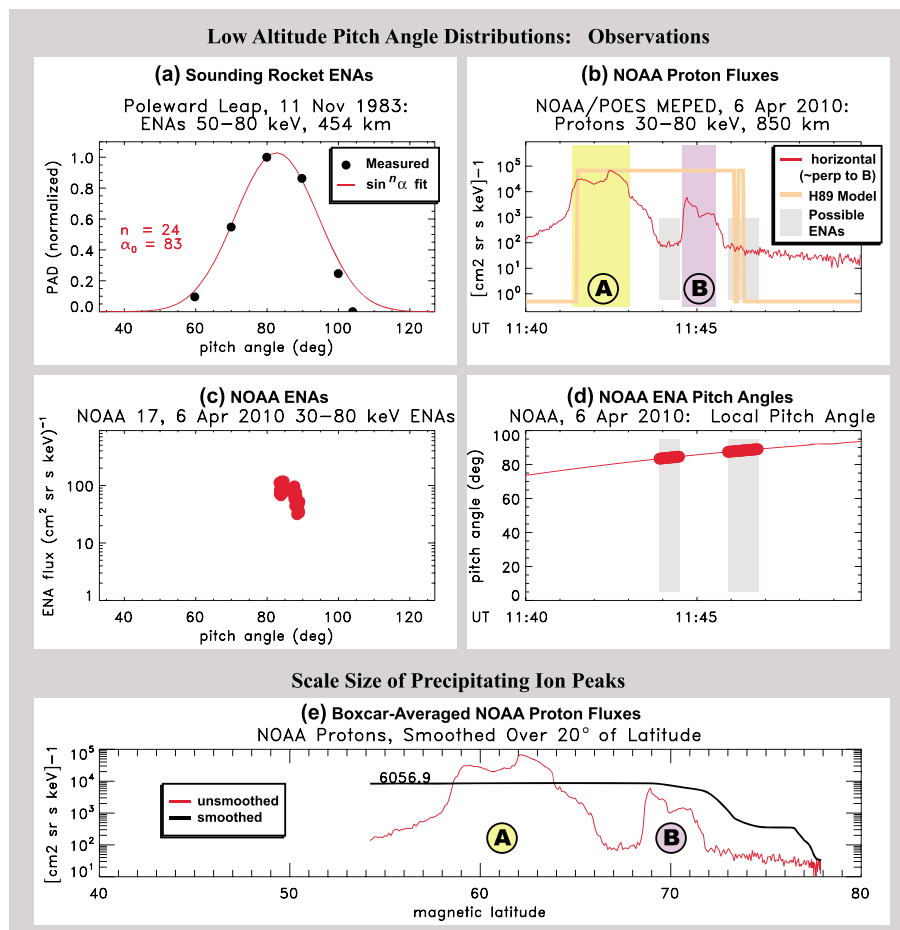


Figure B1. Observations of LAE pitch angle. (a) Poleward Leap rocket-measured ENAs versus pitch angle. (b) NOAA 17 fluxes of two proton peaks (A and B) with possible ENAs in gray boxes and proton oval of empirical model (thick salmon line, cf. Appendix A) normalized to peak A. (c) NOAA ENAs versus pitch angle. (d) NOAA ENA pitch angle versus UT. (e) Boxcar-averaged NOAA protons.

case interval of 6 April 2010, at the approximate location of the TWINS 2 emissivity crescent. Figure B1b shows 30–80 keV NOAA 17 proton fluxes at 820 km, between 1138 and 1148 UT, recorded by the Medium Energy Proton and Electron Detector (MEPED). MEPED samples pitch angle with only two directional channels: roughly perpendicular to the field line (“horizontal,” red curve) and roughly parallel to the field (“vertical/downward,” not shown). In this paper we consider the horizontal detector only since downward moving ions are less likely to produce emergent ENAs. There are two pronounced peaks (A and B) in proton flux that are further discussed in section 5. These peaks apparently span the latitudinal width of the global ion precipitation oval, as represented by the H89 empirical model [Hardy *et al.*, 1989, cf. section A]. In Figure B1b, the full width at half maximum (FWHM) extent of the H89 global oval is given by the thick salmon line. The earlier peak A edge (1141–1142 UT) and the later peak B edge (1145–1146 UT) are both in approximate agreement with the H89 global oval boundaries.

The MEPED instrument is sensitive to neutral particles as well as protons; the gray boxes indicate intervals of possible ENAs [Søråas and Sørbø, 2013] that are identifiable by softer spectra than the precipitating ion peaks A and B. Within these gray boxes the MEPED horizontal (red) ENA fluxes are in the range 30–120 [cm² sr s keV]⁻¹, with a mean value of 70 [cm² sr s keV]⁻¹. It is worth noting that this MEPED ENA flux range overlaps the corrected TWINS 2 ENA flux range (within the same MLT span as the gray boxes): 50–170 [cm² sr s keV]⁻¹, with a mean value of 110 [cm² sr s keV]⁻¹ (cf. blue circles below pixels 9 and 10 of Figure 9a). If it were possible to obtain an ENA pitch angle distribution from these data, the NOAA POES observations might offer a complementary measurement of downward moving ENA PAD. Figure B1d plots the actual pitch angles sampled by MEPED, and Figure B1c shows the resultant (normalized) flux versus α distribution, obtained by gathering all

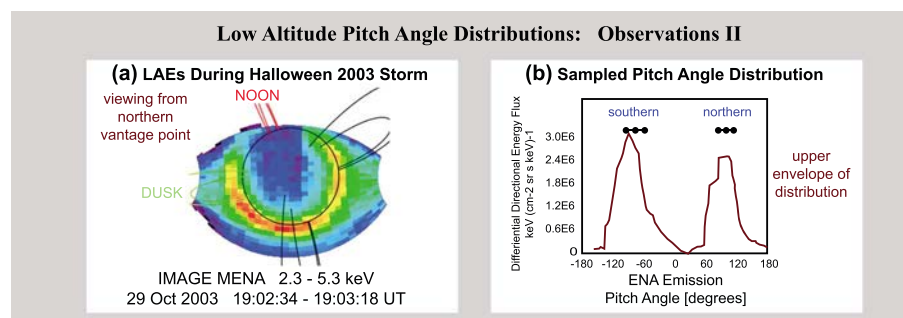


Figure B2. Imaging observations of LAE pitch angle, adapted from Pollock *et al.* [2009]. (a) High spatial resolution LAEs imaged by IMAGE MENA, 19 October 2003, across a much larger fraction of the limb than TWINS viewing geometry can capture. (b) ENA flux (2–5 keV) versus sampled pitch angle.

points from within the intervals bounded by the gray boxes. It is evident by inspection that the NOAA/POES MEPED's limited sampling of PAD is probably insufficient to locate the peak or measure the width of the peak and thus cannot satisfactorily constrain the PAD.

The two peaks A and B are smaller than the TWINS instrument can resolve. As shown in Figure 9b, TWINS 4° angular pixels can span tens of degrees of latitude. Figure B1e plots NOAA proton fluxes from 1138 to 1148 UT, boxcar-averaged over 20° of latitude. The plot is annotated with the average flux value over the entire interval: $\sim 6000 [\text{cm}^{-2} \text{sr s keV}^{-1}]$. The 20° wide boxcar window is still smaller than the largest latitude spans of TWINS pixels. Moreover, the two peaks A and B actually lie within the MLT ranges of two different TWINS pixels, so it is arguable that smoothing these two peaks together does not provide a more direct comparison with TWINS. However, the plot does demonstrate the effect of averaging smaller-scale structures over ionospheric spatial scales comparable to those subtended by TWINS pixels.

Pollock *et al.* [2009] obtained an empirical characterization of a spatially averaged low-altitude ENA pitch angle distribution, using ENA data from two near-perigee passes of the Imager for Magnetopause-to-Aurora Global Exploration (IMAGE) spacecraft during the Halloween 2003 storm. From near-perigee vantage points, the IMAGE Medium Energy Neutral Atom (MENA) camera recorded high spatial resolution LAEs, spanning a much larger fraction of the limb than TWINS captures from its typical vantage point (cf. Figure B2a). Combining images from northern and southern vantage points, Pollock *et al.* compiled distributions of low-altitude ENA flux versus sampled pitch angle for the northern and southern limbs. The upper envelopes (Figure B2b) of the MENA flux distributions are sharply peaked at pitch angles corresponding to upward moving particles. The average pitch angles for the two (northern and southern limb) distributions were found to be $98^\circ \pm 15^\circ$ and $77^\circ \pm 18^\circ$, respectively. The PA range and upper envelopes of these distributions are very similar to the energetic neutral PADs obtained from the Monte Carlo simulation (section 3.1).

The MENA-derived distributions must be interpreted carefully, because of the LAE viewing geometry effect. As described in section 2.3, the difference between sampled PA and the local particle PAD becomes important here: an ENA imager line of sight does not necessarily sample the peak of the local PAD. If the viewing geometry was such that some limb pixels did indeed capture the peak of the PAD, then the local PAD could be represented by the upper envelope of the distribution, plotted in Figure B2b. To make this interpretation based on LAE fluxes sampled across a large fraction of the limb requires the assumption that low-altitude ENA pitch angle distributions do not have a strong spatial dependence (section 3.2).

Acknowledgments

This project was supported by the NASA Heliophysics Guest Investigator program under NNX14AC14G and by the TWINS mission as a part of NASA's Explorer Program. D.B. and V.S. acknowledge support by the Russian Science Foundation (project 14-12-01048). J.C.G. acknowledges support by a research grant from the Belgian Fonds de la Recherche Fondamentale Collective (FRFC). TWINS data used in this paper are publicly available at <http://twins.swri.edu>. NOAA data are publicly available at <http://www.ngdc.noaa.gov>.

References

- Bai, C., R. Conwell, H. Babla, and J. Kindem (2011), Improving image resolution using oversampling for pixelated solid-state Gamma cameras, *J. Nucl. Med.*, *52*, 489.
- Basu, B., J. R. Jasperse, R. M. Robinson, R. R. Vondrak, and D. S. Evans (1987), Linear transport theory of auroral proton precipitation: A comparison with observations, *J. Geophys. Res.*, *92*, 5920–5932, doi:10.1029/JA092iA06p05920.
- Bazell, D., E. Roelof, T. Sotirelis, P. Brandt, H. Nair, P. Valek, J. Goldstein, and D. McComas (2010), Comparison of TWINS images of low-altitude emission (LAE) of energetic neutral atoms with DMSP precipitating ion fluxes, *J. Geophys. Res.*, *115*, A10204, doi:10.1029/2010JA015644.
- Brandt, P. C., S. Barabash, E. C. Roelof, and C. J. Chase (2001a), Energetic neutral atom imaging at low altitudes from the Swedish microsatellite Astrid: Observations at low (≤ 10 keV) energies, *J. Geophys. Res.*, *106*, 24,663–24,674, doi:10.1029/2000JA900119.
- Brandt, P. C., S. Barabash, E. C. Roelof, and C. J. Chase (2001b), Energetic neutral atom imaging at low altitudes from the Swedish microsatellite Astrid: Extraction of the equatorial ion distribution, *J. Geophys. Res.*, *106*(A11), 25,731–25,744.

- Brandt, P. C., D. G. Mitchell, E. C. Roelof, S. M. Krimigis, C. P. Paranicas, B. H. Mauk, J. Saur, and R. DeMajistre (2005), ENA imaging: Seeing the invisible, *Johns Hopkins APL Tech. Dig.*, 26(2), 143–155.
- Buzulukova, N., M.-C. Fok, E. C. Roelof, J. Redfern, J. Goldstein, P. Valek, and D. J. McComas (2013), Comparative analysis of low-altitude ENA emissions in two substorms, *J. Geophys. Res. Space Physics*, 118, 724–731, doi:10.1002/jgra.50103.
- Frey, H. U., S. B. Mende, S. A. Fuselier, T. J. Immel, and N. Østgaard (2003), *Proton Aurora in the Cusp During Southward IMF*, vol. 108, 1277.
- Fruchter, A. S., and R. N. Hook (2002), Drizzle: A method for the linear reconstruction of undersampled images, *Publ. Astron. Soc. Pac.*, 114, 144–152, doi:10.1086/338393.
- Galand, M., and A. D. Richmond (1999), Magnetic mirroring in an incident proton beam, *J. Geophys. Res.*, 104, 4447–4455, doi:10.1029/1998JA900123.
- Galand, M., J. Liliensten, W. Kofman, and D. Lummerzheim (1998), Proton transport model in the ionosphere: 2. Influence of magnetic mirroring and collisions on the angular redistribution in a proton beam, *Ann. Geophys.*, 16, 1308–1321, doi:10.1007/s00585-998-1308-y.
- Gérard, J.-C., B. Hubert, D. V. Bisikalo, and V. I. Shematovich (2000), A model of the Lyman- α line profile in the proton aurora, *J. Geophys. Res.*, 105, 15795, doi:10.1029/1999JA002002.
- Gérard, J.-C., B. Hubert, M. Meurant, V. I. Shematovich, D. V. Bisikalo, H. Frey, S. Mende, G. R. Gladstone, and C. W. Carlson (2001), Observation of the proton aurora with IMAGE FUV imager and simultaneous ion flux in situ measurements, *J. Geophys. Res.*, 106, 28,939–28,948, doi:10.1029/2001JA900119.
- Goldstein, J., and D. J. McComas (2013), Five years of stereo magnetospheric imaging by TWINS, *Space Sci. Rev.*, 180, 39–70, doi:10.1007/s11214-013-0012-8.
- Goldstein, J., P. Valek, D. J. McComas, J. Redfern, and F. Soraas (2013), Local-time dependent low-altitude ion spectra deduced from TWINS ENA images, *J. Geophys. Res. Space Physics*, 118, 2928–2950, doi:10.1002/jgra.50222.
- Hardy, D. A., M. S. Gussenhoven, and D. Brautigam (1989), A statistical model of auroral ion precipitation, *J. Geophys. Res.*, 94, 370–392, doi:10.1029/JA094iA01p00370.
- Hedin, A. E. (1987), MSIS-86 thermospheric model, *J. Geophys. Res.*, 92, 4649–4662, doi:10.1029/JA092iA05p04649.
- Hedin, A. E. (1991), Extension of the MSIS thermospheric model into the middle and lower atmosphere, *J. Geophys. Res.*, 96, 1159–1172.
- Hubert, B., J.-C. Gérard, D. V. Bisikalo, V. I. Shematovich, and S. C. Solomon (2001), The role of proton precipitation in the excitation of auroral FUV emissions, *J. Geophys. Res.*, 106, 21,475–21,494, doi:10.1029/2000JA000288.
- LLera, K., J. Goldstein, D. McComas, and P. Valek (2014), Energy spectral evolution of precipitating ring current ions using TWINS low-altitude emissions (LAEs) and in-situ NOAA observations, Abstract SM31D-4222 presented at 2014 Fall Meeting, AGU, San Francisco, Calif.
- McComas, D. J., et al. (2009), The Two Wide-angle Imaging Neutral-atom Spectrometers (TWINS) NASA mission-of-opportunity, *Space Sci. Rev.*, 142, 157–231, doi:10.1007/s11214-008-9467-4.
- McComas, D. J., N. Buzulukova, M. G. Connors, M. A. Dayeh, J. Goldstein, H. O. Funsten, S. Fuselier, N. A. Schwadron, and P. Valek (2012), Two Wide-Angle Imaging Neutral-Atom Spectrometers and Interstellar Boundary Explorer energetic neutral atom imaging of the 5 April 2010 substorm, *J. Geophys. Res.*, 117, A03225, doi:10.1029/2011JA017273.
- Mitchell, D. G., P. C. Brandt, E. C. Roelof, D. C. Hamilton, K. C. Retterer, and S. Mende (2003), Global imaging of O^+ from IMAGE/HENA, *Space Sci. Rev.*, 109, 63–75, doi:10.1023/B:SPAC.0000007513.55076.00.
- Newell, P. T., T. Sotirelis, and S. Wing (2010), Seasonal variations in diffuse, monoenergetic, and broadband aurora, *J. Geophys. Res.*, 115, A03216, doi:10.1029/2009JA014805.
- Pollock, C., et al. (2001), First medium energy neutral atom MENA images of Earth's magnetosphere during substorm and storm-time, *Geophys. Res. Lett.*, 28, 1147–1150.
- Pollock, C. J., A. Isaksson, J.-M. Jahn, F. Soraas, and M. Sørbø (2009), Remote global-scale observations of intense low-altitude ENA emissions during the Halloween geomagnetic storm of 2003, *Geophys. Res. Lett.*, 36, L19101, doi:10.1029/2009GL038853.1987.
- Roelof, E. C., and A. J. Skinner (2000), Extraction of ion distributions from magnetospheric ENA and EUV images, *Space Sci. Rev.*, 91, 437–459.
- Søråas, F., and K. Aarsnes (1996), Observations of ENA in and near a proton arc, *Geophys. Res. Lett.*, 23, 2959–2962, doi:10.1029/96GL02821.
- Søråas, F., and M. Sørbø (2013), Low altitude observations of ENA from the ring current and from the proton oval, *J. Atmos. Sol. Terr. Phys.*, 99, 104–110, doi:10.1016/j.jastp.2012.10.003.
- Strickland, D. J., R. E. Daniell Jr., J. R. Jasperse, and B. Basu (1993), Transport-theoretic model for the electron-proton-hydrogen atom aurora: 2. Model results, *J. Geophys. Res.*, 98, 21,533–21,548, doi:10.1029/93JA01645.
- Valek, P., P. C. Brandt, N. Buzulukova, M.-C. Fok, J. Goldstein, D. J. McComas, J. D. Perez, E. Roelof, and R. Skoug (2010), Evolution of low altitude and ring current ENA emissions from a moderate magnetospheric storm: Continuous and simultaneous TWINS observations, *J. Geophys. Res.*, 115, A111209, doi:10.1029/2010JA015429.
- Valek, P. W., J. Goldstein, D. J. McComas, R. Iiie, N. Buzulukova, M.-C. Fok, and J. D. Perez (2013), Oxygen-hydrogen differentiated observations from TWINS: The 22 July 2009 storm, *J. Geophys. Res. Space Physics*, 118, 3377–3393, doi:10.1002/jgra.50204.
- Valek, P. W., J. Goldstein, D. J. McComas, M. Fok, and D. G. Mitchell (2014), Large magnetic storms as viewed by TWINS: A study of the differences in the medium energy ENA composition, *J. Geophys. Res. Space Physics*, 119, 2819–2835, doi:10.1002/2014JA019782.
- Valek, P. W., J. Goldstein, J.-M. Jahn, D. J. McComas, and H. E. Spence (2015), First joint in situ and global observations of the medium-energy oxygen and hydrogen in the inner magnetosphere, *J. Geophys. Res. Space Physics*, 120, 7615–7628, doi:10.1002/2015JA021151.